Torsional electromechanical systems based on carbon nanotubes

Torsional electromechanical systems based on carbon nanotubes

A R Hall[1]**, S Paulson**[2]**, T Cui**[3]**, J P Lu**[3,4]**, L-C Qin**[3,4]** and S Washburn**[3,4,5,6]

[1] Joint School of Nanoscience and Nanoengineering, University of North Carolina Greensboro, Greensboro, NC 27401-4901, USA

[2] Department of Physics and Astronomy, James Madison University, Harrisonburg, VA 22807-0001, USA

[3] Department of Physics and Astronomy, University of North Carolina at Chapel Hill, Chapel Hill, NC 27599-3255, USA

[4] Curriculum in Applied Sciences and Engineering, University of North Carolina at Chapel Hill, Chapel Hill, NC 27599-3255, USA

[5] Department of Computer Science, University of North Carolina at Chapel Hill, Chapel Hill, NC 27599-3255, USA

[6] Department of Biomedical Engineering, University of North Carolina at Chapel Hill, Chapel Hill, NC 27599-3255, USA

E-mail: adam.hall@uncg.edu

Abstract
Carbon nanotubes (CNTs) are among the most highly studied nanomaterials due to their unique (and intertwined) mechanical and electrical properties. Recent advances in fabrication have allowed devices to be fabricated that are capable of applying a twisting force to individual CNTs while measuring mechanical and electrical response. Here, we review major results from this emerging field of study, revealing new properties of the material itself and opening possibilities for advances in future devices.

(Some figures may appear in colour only in the online journal)

Contents

List of symbols

a_{C-C}	inter-atom spacing on the graphene lattice
$\boldsymbol{a}_i$	unit vectors in the graphene lattice
AFM	atomic force microscopy
BHF	buffered hydrofluoric acid
$C, \boldsymbol{C}_h$	lattice translation vector
CNT	carbon nanotube
CVD	chemical vapor deposition
D_i	line spacing
DWNT	double-wall nanotube
E	energy, Young's modulus
EBL	electron beam lithography
F	total scattering amplitude
F	atomic scattering amplitude
F	friction force
FIB	focused-ion beam
G	shear modulus
I	scattering intensity
J_n	Bessel function
$\boldsymbol{k}, k$	reciprocal lattice vector
k	Boltzmann's constant
K_T	spring constant
L	*length*
MWNT	multi-wall nanotube
NEMS	nano-electro-mechanical system
p, q	integers
R	resistance, radial coordinate in reciprocal space
R	nanotube radius, radial coordinate
S	slope
SEM	scanning electron microscope
SWNT	single-wall nanotube
t	shell thickness, transmission coefficient
t_0	hopping amplitude
T	temperature, torque
TEM	transmission electron microscope
u, v	chiral vector indices
V	Coulomb potential
W	work
γ	shear strain
ε_0	dielectric permittivity
θ	chiral angle for nanotube lattice
ϕ	twist angle
σ	surface charge density, axial strain

1. Introduction

Over the past two decades, carbon nanotubes [1, 2] (CNTs) have been the subject of intense theoretical and experimental investigation. The interest in CNT arises because they have electrical and mechanical properties that rival the best available in nature, and hence a great deal of commercial potential. This interest has been fueled by the unusual electrical, structural and mechanical properties they possess. These properties make CNT ideal structures for studies of fundamental properties of nanometer sized and reduced dimension systems, as well as promising candidates for technological applications.

This review presents recent advances in the fabrication, measurement and theoretical study of the electrical and mechanical response to nanotubes which have been twisted along their axis of symmetry. In this section, we begin with a discussion of the structure and properties of CNT, as well as their utility in uniaxial electromechical devices. In section 2, we will review theory and experiments pertaining to torsional mechanics of individual CNT. Section 3 discusses the electromechanical response to applied torsional strain in CNT devices. Section 4 will focus on torsional experiments performed *in situ* in a transmission electron microscope. Finally a perspective on future directions will be shared.

1.1. CNT structure

The atomic structure of a CNT is visualized by taking a rectangular portion from a graphene sheet and rolling it into a seamless cylinder. The two-dimensional graphene lattice consists of a two-atom (A and B) unit cell which is the basis for a hexagonal lattice with unit vectors $\boldsymbol{a}_1 = a_{C-C}(\sqrt{3}, 0)$ and $\boldsymbol{a}_2 = a_{C-C}(\sqrt{3}/2, 3/2)$, where $a_{C-C} = 0.142$ nm is the carbon–carbon bond length (figure 1(*a*)). The width of the graphene sheet forming the nanotube is defined by a combination of unit vectors known as the chiral vector, $\boldsymbol{C}_h = u\boldsymbol{a}_1 + v\boldsymbol{a}_2$, where u and v are integers. Upon rolling the sheet into a cylinder the chiral vector will outline the circumference of the CNT. The specific values of u and v will determine the circumference of the tube as well as the chiral angle θ, which can range from $0°$–$30°$. The diameter, chiral angle and electrical properties of CNT are described solely by the variables u and v. Specific CNT are therefore referred to as (u, v); in the highly symmetric cases when $u = v$ the CNT is referred to as an armchair nanotube, and a zigzag CNT when $v = 0$; all other CNT are referred to as chiral.

The simplest form of CNT—a single graphitic layer— is referred to as a single-wall CNT (SWNT, figure 1(*b*)). CNT, however, exists also in another morphology, consisting of nested cylinders with spacing between shells of about 0.34 nm, similar to the spacing between layers in graphite. This variety of nanotube is referred to generally as multi-wall CNT (MWNT) (figure 1(*c*)). In practice, the number of shells in a MWNT ranges from two (referred to as a double-wall CNT or DWNT) to several tens.

1.2. CNT electrical properties

One of the more intriguing aspects of CNT is seen when calculating the electronic band structure. A π-orbital, nearest-neighbor tight-binding calculation of the band structure demonstrates that graphene is a semimetal, with six points at the corners of the Brillouin zone comprising the Fermi surface [3]. The energy band diagram produced by this model is shown in figure 2(*a*) and given by

$$E = \pm t_0 \left[1 + 4\cos\left(\frac{3}{2}k_y a_{C-C}\right)\cos\left(\frac{\sqrt{3}}{2}k_x a_{C-C}\right) \right.$$
$$\left. + 4\cos^2\left(\frac{\sqrt{3}}{2}k_x a_{C-C}\right) \right]^{1/2}, \tag{1.1}$$
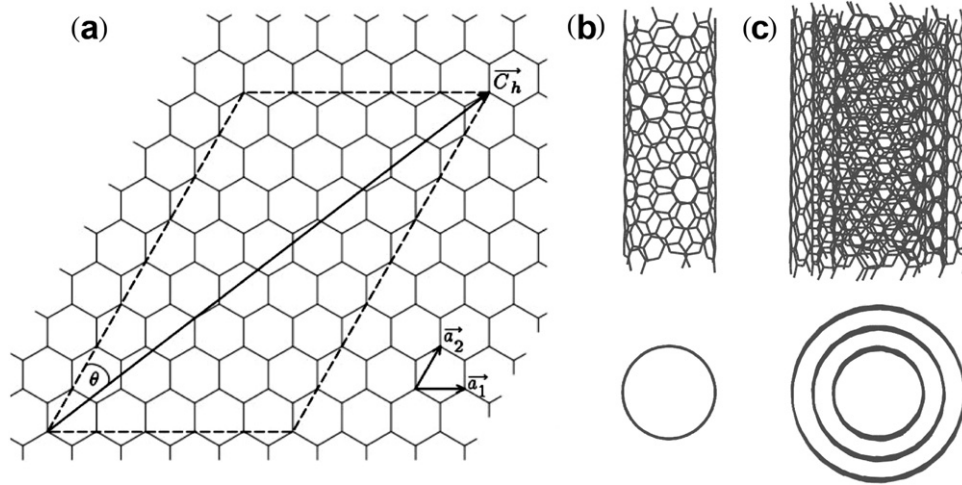
Figure 1. (*a*) Representation of an infinite graphene sheet showing the unit vectors a_1 and a_2 in real space. The chiral vector $C_{\rm h}$ represents a wrapping of the two-dimensional graphene sheet into a tubular form. The chiral angle is θ. Also shown are representations (top: side view; bottom: cross-section) of (*b*) a SWNT (chiral indices (8,5)) and (*c*) a MWNT with three shells.
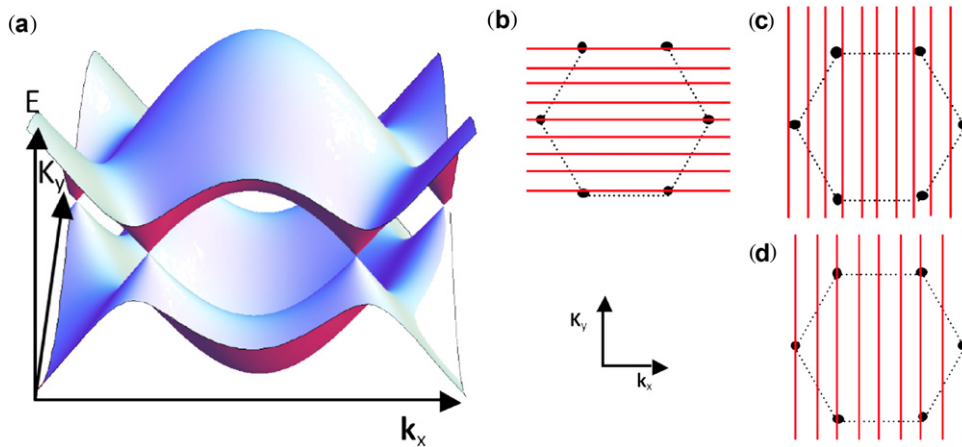
Figure 2. (*a*) π orbital tight binding structure of graphene. The Fermi surface consists of six points at the corners of the hexagonal Brillouin zone. (*b*)–(*d*) The red lines depict the states allowed by the periodic boundary condition imposed by rolling the graphene sheet into a cylinder. Examples are shown for an armchair (*b*) and semiconducting (*c*) and metallic (*d*) zigzag CNT.

where t_0 is the nearest-neighbor π-orbital hopping parameter, and (k_x, k_y) is the 2D wave vector. To determine the electronic structure of a nanotube, rolling the graphene sheet into a cylinder imposes a periodic boundary condition allowing only electrons with wavevectors k that satisfy $C \cdot k = 2\pi q$ (q an integer). Specific values of (u, v) determine C, and therefore the allowed values for k. This results in 1D slices of allowed states through the 2D graphene band structure. These slices are the 1D electronic bands for the CNT. In this model, if the condition that $2u + v = 3p$ (for integer p) is met, the allowed states will include the Fermi points, and thus these CNT are metallic; all other CNT will be semiconducting [4–6]. Figures 2(*b*)–(*d*) show these states for the high symmetry armchair and zigzag CNT. Near the Fermi level, the energy dispersion of graphene band structure is linear, and as a result the band gap of semiconducting SWNTs varies inversely with the tube diameter

$$E_{\rm g}^{(0)} = \frac{t_0 a_{\rm C-C}}{r}, \qquad (1.2)$$

where r is the radius of a SWNT [7, 8].

The finite curvature of nanotubes induces hybridization of σ- and π-states and modifies both the length and angle of bonds between two neighboring carbon atomic orbitals, such effect is significant for small radius CNTs and can cause the opening of a secondary band gap [9]. This secondary band gap scales with the inverse of tube radius squared and is sensitive [10] to the chiral angle θ,

$$E_{\rm g}^{(1)} = \frac{3t_0 a_{\rm C-C}^2}{16r^2} \sin 3\theta. \qquad (1.3)$$

For semiconducting nanotubes, this hybridization-induced correction to the band gap is negligible. For small metallic nanotubes, however, the curvature effect is important, as shown in figure 3. An exception is the armchair tube, which remains metallic due to its unique symmetry.

Individual shells of a MWNT are bound by these same conditions. In practice, however, large MWNT tend to exhibit metallic characteristics due to large outer diameter and possible inter-shell interactions [11]. Small MWNT and DWNT would
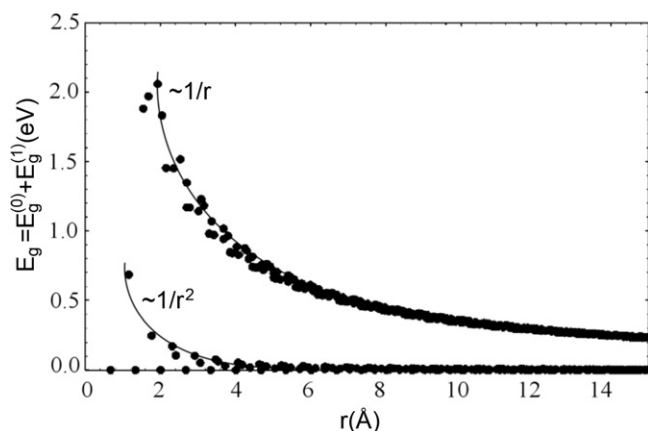
Figure 3. The band gaps of semiconducting (top) and 'metallic' (bottom) nanotube as a function of tube radius. The solid lines are a guide to the eye showing that the primary band gap $E_g^{(0)}$ scales a $1/r$, and the curvature induced hybridization secondary band gap $E_g^{(1)}$ scales as $1/r^2$. Notice $E_g^{(1)}$ is significant only for small 'metallic' tube and that it is zero for armchair tubes. After [103].

be expected to show more intricate behavior, varying based on the structures of (and interactions between) individual shells.

1.3. Axial electromechanical CNT devices

The strength and small size of CNT make them attractive candidates for inclusion in a number of electromechanical devices. A widely studied example of this uses a mechanical response to an applied electric field to realize mechanical resonance in the CNT. The first realization of such devices [12] consisted of singly clamped MWNTs several micrometers long with resonance frequencies in the range 1 to a few MHz. These devices operated inside of a TEM to allow the direct observation of the mechanical resonance.

Sazonova *et al* [13] fabricated a mechanical oscillator from a doubly clamped SWNT, with a micrometer-sized section suspended over an electrostatic gate, which was used to drive the resonator (figure 4). Using the CNT as a mixer, this group was able to detect electrically the resonance of the CNT through the change in capacitance with the gate. This change was only noticeable for large displacements of the tube; that is, when the tube is vibrating at its resonant frequency. Furthermore, by applying a dc voltage to the gate, they demonstrated control over the tension in the CNT and changed the resonance by a factor of two or more.

The high resonant frequency and low mass of CNT oscillator systems make them ideal candidates for sensitive mass detectors. Several groups [14–16] used CNT electromechanical oscillators to detect the absorption of individual atoms and their masses. The measured resonant frequency decreased as mass accumulated on the CNT sensor. In each of these experiments the limit of detection of the sensor was at or near the mass of an individual atom. In one case [15] this was demonstrated at room temperature.

A novel use of the electromechanical response of a CNT was the creation of a fully functioning radio in which the nanotube acted as the antenna, tuner, amplifier and demodulator [17]. Figure 5 shows a schematic of the radio device. As seen in previous CNT electromechanical oscillators, an ac electric field that is tuned to the resonant frequency of the CNT will cause the nanotube to resonate mechanically. The resonant frequency of the CNT device depends on its length and the tension in the CNT, and control of both was demonstrated in this experiment. Course adjustment, or trimming, of the resonant frequency was obtained by running a high field emission current through the CNT. This process ejected carbon atoms from the end of the nanotube, permanently shortening the length, and therefore increasing the resonant frequency until the approximate desired frequency was acquired. Fine-tuning was accomplished by applying a voltage to a counter electrode that increased or decreased the tension in the CNT. This process was repeatable and was used to tune the resonant frequency of the CNT by approximately 5%. A field emission current was driven from the CNT to a counter electrode. This field emission current was modulated by mechanical motion, and thus the (mechanically) received signal was transformed back into an electrical signal and then amplified.

The discussion thus far has been limited to uniaxial and radial deformations, and devices based on these. Another mode of operation is torsional deformation, which may hold potential for miniaturization of specific types of nanoelectromechanical systems such as variable capacitors and high-switching speed mirrors. In this review paper we will present theoretical and experimental work probing the mechanical and electromechanical response of CNT to torsional strain.

2. The CNT torsional device: general fabrication

Devices incorporating an individual SWNT, DWNT or MWNT as a torsional element all have the same basic architecture: a section of nanotube pinned at its ends and unsupported locally by substrate bears a small metal block at its center (figure 6). The block can be used as a lever for applying a torsional strain to the nanotube. This design was motivated by previous work on larger microelectromechanical paddle oscillators [18] that were monolithic structures built entirely from silicon. The integration of a nanotube in the device, however, requires additional methods beyond the common microfabrication techniques used in this earlier work. Here, we discuss several factors central to general torsional device fabrication. Modifications to this general procedure necessary for specific measurements will be described briefly in later sections.

2.1. CNT deposition and growth

For MWNT devices [19–23], nanotubes made with either the laser ablation method [24] or the arc discharge method [25] are used. The raw material is suspended in a non-polar solvent such as dichloromethane [23] or 1,2 dichlorobenzene [21] and subjected to an ultrasonic treatment in order to break up densely packed bundles. MWNT can be introduced randomly on a substrate by depositing a $\sim15\,\mu$L drop of suspension
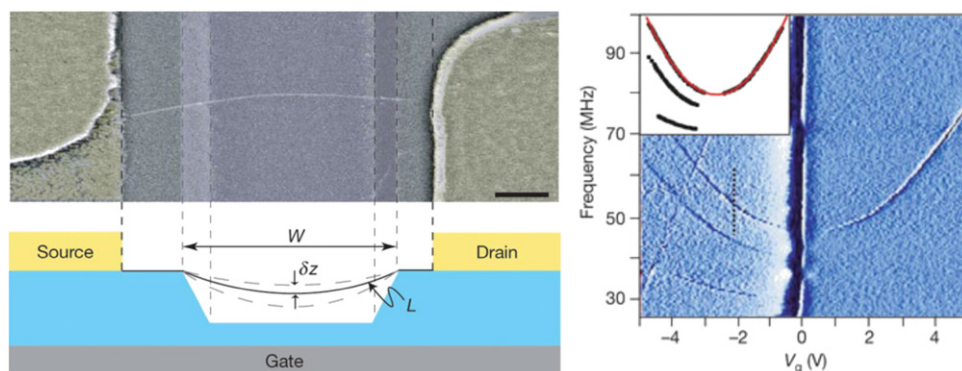
Figure 4. (*a*) False-color SEM image of suspended CNT mechanical resonator. An ac voltage applied to the gate at the CNT resonant frequency drives the motion of the resonator. A dc component of the gate voltage can be used to attract (or repel) the CNT and thereby control the tension, and thus the resonant frequency. (*b*) The differential conductance of the CNT as a function of the dc gate voltage and drive frequency. The white peak corresponds to the resonance of the oscillator. Reproduced with permission from [13]. Copyright 2004 Nature Publishing Group.
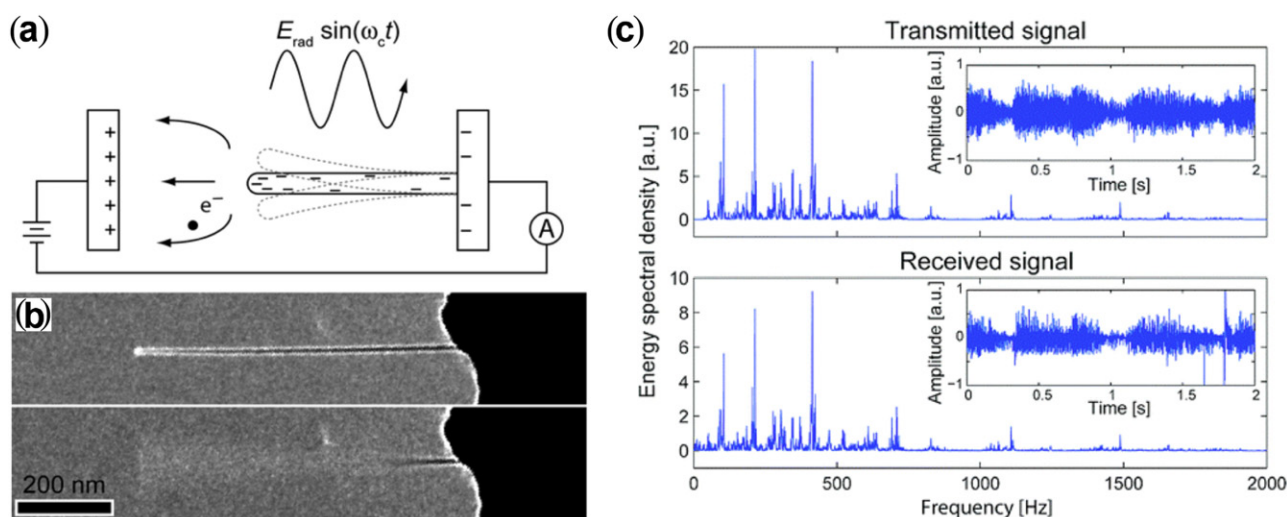
Figure 5. (*a*) Schematic of a nanotube radio. The length and tension of the CNT oscillator tune the radio to pick up only the desired frequency. The received signal is measured via the field emission current between the end of the CNT and a counter electrode. (*b*) Electron micrograph of a nanotube radio off (top) and on (bottom) resonance. (*c*) Spectra and waveforms (inset) of the transmitted received signal. Image courtesy of Zettl Research Group, University of California at Berkeley, and Lawrence Berkeley National Laboratory. Reproduced with permission from [17]. Copyright 2007 American Chemical Society.
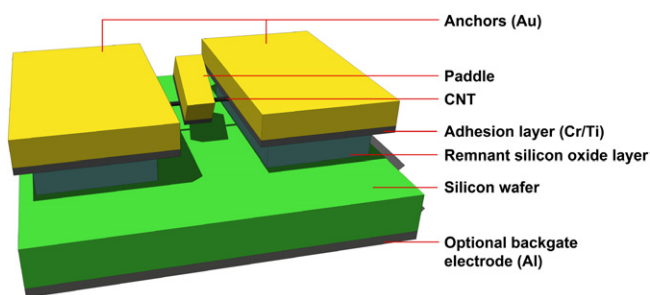
Figure 6. Diagram of a nanotube torsional device. An individual nanotube, pinned at either end by large lithographic pads, supports a small freely suspended block at its center.

on the surface followed by $\sim$50 μL of isoproponol. This addition changes the overall polarity of the solvent, causing the nanotubes to fall out of suspension and onto the underlying surface. An alternative technique uses flow alignment to deposit nanotubes at pre-determined positions [26].

SWNT and DWNT can be produced in bulk with techniques [27, 28] comparable to those used for MWNT. They are, however, more difficult to deposit from liquid, due to their low mass-to-surface area ratio. This results in the formation of ropes rather than individual nanotubes due to van der Waals interactions. One possible solution is the use of surfactants such as sodium dodecylsulfate in water [29], which can create a molecular barrier between nanotubes in solution, but this does not deposit individual nanotubes with absolute certainty [30]. In order to avoid these issues, chemical vapor deposition (CVD) techniques can be used to grow disperse nanotubes directly onto a substrate.

CVD recipes vary considerably, but in a typical growth process, catalyst particles are deposited directly onto a substrate by evaporation of a liquid suspension. In the case of SWNT, Fe/Mo nanoparticles have been shown to be successful catalyst particles [31]; for DWNT, FeSi$_2$ powder can be used [32]. Catalyst density can be controlled in order to create a sparse coverage of nanotubes for device fabrication. The
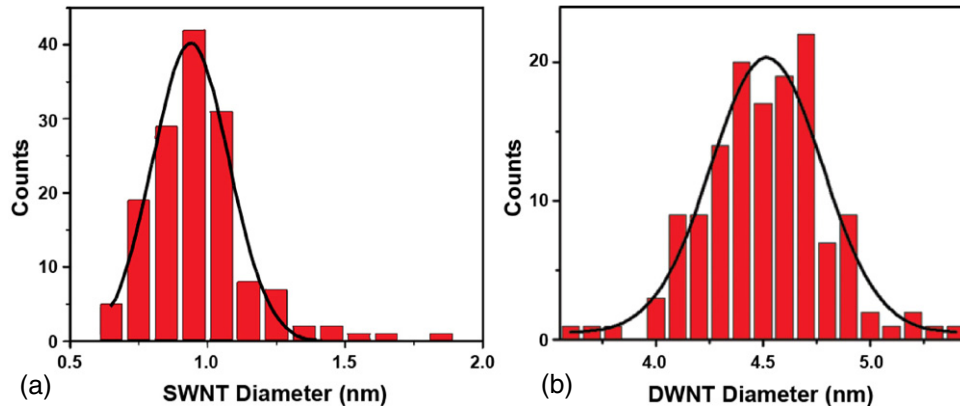
Figure 7. Distribution of nanotube diameter for (*a*) SWNT and (*b*) DWNT, as determined by AFM. In each plot, the solid line is a Gaussian fit to the data. After [32, 91].
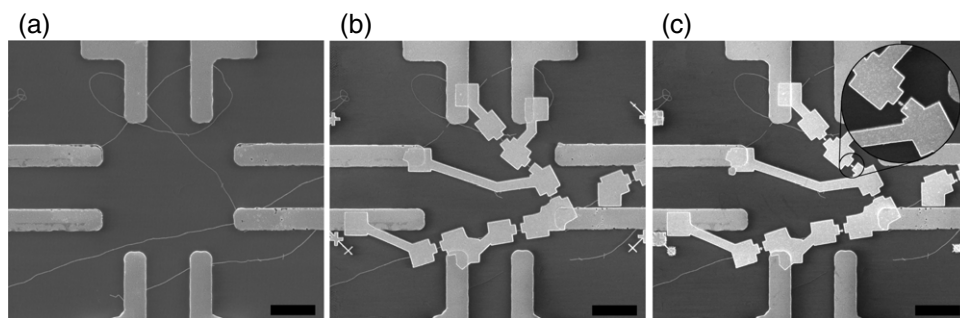
Figure 8. Device fabrication sequence. (*a*) CNTs on an oxidized Si wafer with a photolithographically defined structure. (*b*) EBL definition of large anchor pads on either end of target sections of nanotube and alignment markers (cross-hairs). (*c*) EBL definition of small pads at the center of each target nanotube (inset: magnified view of sample device structure). Scale bars are 10 μm.

substrate is subsequently placed in a tube furnace and exposed to high temperatures (700–900 C) under the controlled flow of feed gases. These consist generally of methane, ethylene and hydrogen in a specific ratio. Following this growth process, the substrate is returned to room temperature to undergo additional fabrication steps. The resulting material is almost entirely composed of well-separated nanotubes with low variability in average diameter (figure 7).

2.2. Torsional device construction

Fabrication of a torsional device requires several steps of lithography in order to make and align structures to the nanotube. On a degenerately doped silicon wafer with a thermally grown oxide layer of 0.5 to 1 μm, common photolithography is performed in order to define surface bound metal pads (typically 10 nm Ti and 30 nm Au). The pattern is designed to converge to an area of $\sim$50 $\times$ 50 μm^2. For devices requiring an underlying (substrate) gate electrode, the oxide layer is removed from the back side of the wafer with a hydrofluoric acid (HF) etch and Al immediately evaporated onto the surface. This makes electrical contact directly to the silicon wafer, separated from the nanotube by only the top oxide thickness. In the case of devices incorporating MWNT, these first fabrication steps are performed prior to nanotube deposition from liquid. With CVD nanotubes, the steps are performed directly following growth in order to avoid thermal damage to the metal pattern.

Next, nanotubes are located with respect to the patterned metal using a scanning electron microscope (SEM, figure 8(*a*)) or an AFM [20]. These images are used to perform electron beam lithography (EBL) on the substrate, fabricating large anchor contacts on either end of target nanotubes (figure 8(*b*)). This step of EBL is also used to pattern fine fiduciary marks (cross-hairs). In some devices [21, 33], additional electrodes can be patterned around the paddle during this step for electrostatic actuation.

Following metal deposition of the primary patterns (typically 10 nm Ti and 50 nm Au), the device area is imaged once again to determine precise locations for all contacted nanotubes. A second step of EBL is performed to fabricate the small paddle structure onto the length of nanotube between each set of large anchor pads (figure 8(*c*)). This step is aligned to the fine cross-hairs for high precision and is used to pattern only the smallest features of the devices, in order to avoid detrimental effects of drift during pattern exposure.

In the final step, buffered HF (BHF) is used to remove 0.5 to 1 μm of oxide (depending on original thickness) selectively from beneath the device. Because BHF is an isotropic etchant and because the paddle is small compared with the anchor pads, a properly timed etch leaves the paddle suspended above the substrate supported only by the nanotube. The device is then dried with supercritical CO_2 in order to prevent collapse due to surface tension effects during evaporative drying.

Table 1. Values of the Young and shear moduli calculated by various groups with different methods. Except for the work of Yakobson *et al* [41], Young's modulus is found to be on the order of 1 TPa. In the calculation of Yakobson *et al* [41] if instead of the π-bond length of 0.66 Å, the van der Waals wall thickness of 3.4 Å is used as the wall thickness, then one obtains Young's modulus of 1.07 TPa, consistent with other calculations.

Authors	Year	Young's modulus E (TPa)	Shear modulus G (TPa)	Potential/method
Robertson *et al* [34]	1992	1.06		Tersoff–Brenner
Yakobson *et al* [41]	1995	5.5		Tersoff–Brenner Continuum
Cornwell and Wille [156]	1997	1		Tersoff–Brenner
Lu [35]	1997	0.97	0.45	Force-constant
Hernández *et al* [36]	1998	1.24		Density-function
Krishnan *et al* [157]	1998	1.3		Thermal vibration
Sánchez-Portal *et al* [37]	1998	1.05		Density-function
Popov *et al* [38]	1999	1.00	0.41	Lattice dynamics
Ozaki *et al* [158]	2000	0.98		O(N) Tight-binding
Van Lier *et al* [159]	2000	1.09		Hartree–Fock
Belytschko *et al* [39]	2002	0.94		Modified Morse
Shen and Li [160]	2003	1.06	0.44	Energy approach
Pullen *et al* [161]	2004	1.1		GGA
Gupta *et al* [162]	2005	1.2	0.35	Tersoff–Brenner

3. CNT torsional mechanics

3.1. Theoretical understanding

The mechanical properties of CNT have been a focal point of many theoretical works. Here, we provide a brief overview of the various simulation and numerical methods used in these investigations.

Using molecular dynamics simulation with Tersoff–Brenner potential for the carbon–carbon interaction, Robertson *et al* [34] first reported Young's modulus E of nanotubes to be smaller than that of the graphene. Using an empirical force-constant model, Lu [35] calculated E for both SWNT and MWNT to be around 1.0 TPa, insensitive to the chirality, the tube size and the number of walls, and comparable to modulus of the graphene, These results were confirmed subsequently with other methods including the tight-binding simulation and density-functional calculation [36, 37], Born's perturbation technique within a lattice-dynamical model [38], as well as using a modified Morse potential [39] and MM3 potential [40].

Using the Tersoff–Brenner potential for SWNT, Yakobson *et al* [41] and Kudin *et al* [42] estimated E to be 5.5 and 3.86 TPa in a continuum elasticity approximation. These values were derived with the assumption that the individual wall thickness is of the size of molecular orbital radius. If the inter-wall van der Waals distance is used, Young's modulus is about 1 TPa, consistent with other calculations. Table 1 is a summary of the elastic modulus calculations with various methods. As can be seen, with few exceptions, the generally agreed value for Young's modulus is around 1 TPa.

Compared with the numerous works for SWNTs, only a few results have been published for MWNT due to the complexity of structures. Lu [35] first calculated E and the shear modulus G of MWNT to be 1.1 TPa and 0.5 TPa, respectively, using a force-constant model and assuming that all the walls are uniformly loaded. It was also shown that the elastic moduli vary little with the number of walls. Li and Chou [43] used the molecular structure mechanics method

to obtain similar values for Young's and shear modulus (see table 1). It is generally agreed that the weak inter-wall van de Waals interaction is not sufficient to transfer the mechanical loading from outer wall to the inner walls. In an analysis of elastic moduli of MWNT by Shen and Li [44], it was shown that the average values of E and G are 1.2 TPa and 0.3 TPa, respectively. For torsional strain it was also reported that a critical torsional angle exists beyond which the stiffness of nanotube is significantly reduced because of buckling [45].

Torsion-induced buckling [46] has itself been investigated theoretically as well for SWNT [47–49], DWNT [50–52] and MWNT [53–55]. These studies show that energy minimization results in morphological helical ripples in each structure under torsion. Complete collapse can also occur, forming ribbon-like structures held together with van der Waals interactions [56–60]. These ribbons can themselves exhibit interesting behaviors. However, structural changes of these kinds are expected to arise only at shear strains above about 5%, which are higher than the range studied commonly in the devices discussed in this review.

An additional factor of interest to the present discussion is the idea that CNT torsion can be coupled to other mechanical and electromechanical stimuli. For instance, as a consequence of symmetry breaking, an applied axial tension can be expected to induce a torsional response in an individual CNT and vice versa [61–64]. Related effects are responsible for the dependence of chiral SWNT torsional properties on the loading direction [65]. Furthermore, electromechanical coupling can have a similar effect as charge injection to or removal from a CNT lattice can affect the carbon–carbon bond distance. In chiral SWNT, for example, this can result in a net torsional deformation [66]. These interesting findings may be of great interest to the field in the future, offering, e.g., new methods by which to actuate devices.

3.2. MWNT

One of the most intriguing results from experiments on torsional strain is one of the oldest. Before the work on

SWNT and DWNT, there were several experiments on MWNT. Both quasi-static [22, 67] and resonance experiments [68] were performed, and in qualitative ways, most of these data agreed with predictions from a variety of theoretical methods from atomistic up through continuum approximations [35, 45, 69–77].

3.2.1. Quasi-static deflections and the modulus of the nanotube. Strain was enforced on MWNT paddle structures similar to the ones discussed below for SWNT (but larger in size having radii around 15 nm). An AFM tip was used, and this allowed for measuring the applied stress [22]. The experiment is depicted schematically in figure 9(*a*). An AFM cantilever depressed the paddle at some point along its length a distance x from the MWNT. In principle this could induce tensile strain as well as torsion strain giving rise to deflections z and θ, respectively. In practice almost all of the induced strain was torsion as expected from the very large tensile force constant K_z compared with the torsion spring constant K_T.

As seen in figure 9(*a*) the force required to deflect the paddle through a certain angle ϕ decreases as x, and the lever arm for the applied torque, increases. From simple mechanical analysis, one expects that the force to deflect the paddle contains a term proportional to K_z plus a term proportional to K_T. As a practical matter it is useful to scale the measured forces against the force constant K_C to deflect the AFM cantilever against a rigid surface such as the substrate of the sample holder. The ratio of these forces is encoded in the slope of the AFM cantilever deflection versus piezotube position Z_P. Analysis of the forces and torques leads to the following ratio [22] of the slope (i.e. force) applied by the cantilever to the paddle S_{paddle} to the slope when the cantilever is deflected by the rigid substrate $S_{\text{substrate}}$

$$\frac{S_{\text{paddle}}}{S_{\text{substrate}}} = \left[1 + \frac{K_C}{K_z} + \frac{K_C x^2}{K_T} \right]^{-1}. \quad (3.1)$$

The data in figure 9(*b*) agree nicely with this prediction. The figure shows two sweeps of the AFM tip along the paddle with fits of this equation to the measurements. As a consequence of the fit we can assert that the second term is negligible, which is not surprising as the tensile modulus of the MWNT is very large compared with the cantilever modulus [35].

The values of the two spring constants of the MWNT can be evaluated easily in a classical approximation [78] based on presumed knowledge of Young's modulus E and shear modulus G. Because of some technical difficulties the experiment could not measure K_z, but some detailed measurements of K_T were carried out. The torsion spring constant is

$$K_T = \pi G (r_o^4 - r_i^4)/2l, \quad (3.2)$$

where l is the sum of lengths of the MWNT segments connecting the paddle to the anchors, and r_o and r_i are the outer and inner radii, respectively. From this formula we can extract the shear modulus G if we know the inner radius. This is difficult to measure without TEM, which was not used in this experiment. Fortunately substantial variations in r_i have only a
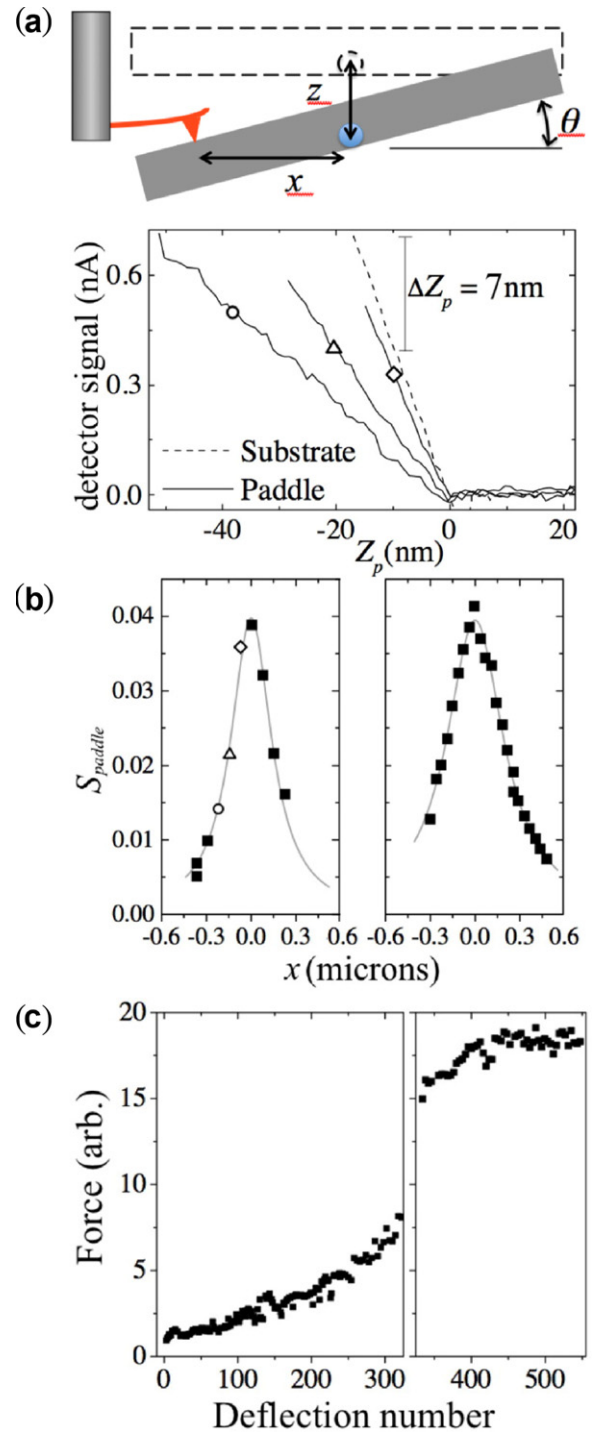
Figure 9. (*a*) Top: schematic of possible deflections; bottom: representative force–distance curves for deflections at different locations on a paddle. (*b*) Earlier and later deflections forces versus location along the paddle. (*c*) Deflection force at a certain location as a function of the number of deflections. The MWNT had an outer diameter of about 16 nm. Adapted with permission from [22]. Copyright 2002 American Physical Society.

small effect on the result so long as r_i is smaller than about $r_o/2$, which was typical for the MWNT in these experiments [22].

In figure 9(*b*), the data on the left were an earlier sweep than the data on the right, and both can be modeled with equation (3.2). The intriguing aspect is that the later sweep

implies a significantly larger value of K_T. For the earlier sweep the value of K_T is about 40 fN m, but it is more than 70 fN m for the later sweep. This increase is completely unexpected and still somewhat mysterious. Theoretical modeling in both continuum [72–74, 79] and atomistic methods [77, 80–82] suggests that defects linking the shells might develop as a result of the relative motion and strain on the individual shells. This conclusion remains speculative until experiments confirm the change in defect structure that is responsible. Other theoretical work suggests the importance of tensile strain as a possible mechanism that stiffens the torsional response [45, 76]. In another experiment, a paddle was deflected hundreds of times and after about 400 deflections the increase in K_T saturated at a value about an order of magnitude above the initial response (figure 9(*c*)). Qualitatively, one can say that at first the shells rotate independently of each other or with low friction as suggested in DWNT experiments (see below). As strain is applied repeatedly, defects form that lock the shells together more rigidly, and finally the whole structure twists as a thick solid cylinder. Neither the nature of these defects nor the thermodynamics of their formation is understood for certain.

Circumstantial evidence for the links among shells can be found in the results for the inferred shear modulus. The value of G has been calculated carefully and the result is 0.54 TPa [35]. In the experiments, the inferred values from the first few deflections on any given device were typically a factor of 10–100 lower—if the MWNT is assumed to behave as a solid cylinder. On the other hand if only the outer shell contributed to the shear modulus, then the inferred value is within a factor of two or so of the predicted value. In contrast, after many deflections the inferred modulus reflected shear strain in the entire solid cylinder comprising all of the shells. The obvious conclusion is that in the unstrained MWNT, the shells shear more or less independently from each other, but after repeated strain, the shells are linked so that the whole structure behaves as a thick cylinder with about the same shear modulus as the individual CNT.

Other experiments on quasi-static torsional strain in MWNT have been performed, but there are no observations of this kind of 'work hardening' in those reports [83].

3.2.2. Resonance oscillations. Resonance frequencies of MWNT-based paddle oscillators were very high for detection with garden-variety AFM methods (although more exotic force sensing methods have been used [84] at high frequencies). The detection of torsional resonance oscillations in paddle oscillators has been carried out typically either with detection of changes in capacitance [85], piezoresistive response as discussed below [86], or with optical scattering [68].

In the first experiments on MWNT resonance, the oscillations were driven by an alternating electric field between the substrate (or 'back gate'), and the paddle. An extra constant electric field was added to bias the deflection of the paddle [68]. For a paddle oscillator the resonance is expected near a frequency

$$\omega_R = \sqrt{\frac{K_T}{I}}, \qquad (3.3)$$

where I is the moment of inertia of the paddle about an axis along the center of the MWNT. (The moment of the MWNT is negligible by comparison.) Of course this is the expectation from a linear approximation of the rather complicated potential from the atoms within each shell and the interactions among the shells. The torsional component of the potential $U(\phi)$ certainly is not a simple parabola and may well have a very complicated structure from commensuration effects. It is obvious from elementary analysis that the potential

$$U(\phi) = \frac{1}{2!}\frac{\partial^2 U}{\partial \phi^2}\phi^2 + \frac{1}{3!}\frac{\partial^3 U}{\partial \phi^3}\phi^3 + \frac{1}{4!}\frac{\partial^4 U}{\partial \phi^4}\phi^4 + \cdots \qquad (3.4)$$

can have nonlinear terms, and hence, that the resonance can have very complicated behavior depending on which term dominates at a particular amplitude of deflection. The resonance frequency above is just the result of the first term. In the experiments [68], different trends are obtained in different oscillators. For example data in figure 10(*a*) illustrate the classic hysteretic jump between amplitudes when driven hard. It also indicates that the potential first tends to soften and the resonance shift to lower frequency as the drive amplitude (and hence the oscillation amplitude) increases. In contrast the resonance of another oscillator (figure 10(*b*)) shifts to higher frequency before beginning to retreat. Theoretical understanding of this difference in trend is only qualitative at this time.

Inferred values of G from the resonance frequencies might have been expected to fall into the 'thick cylinder' scheme discussed above, because the resonating structure per force has already undergone a few million deflections as the measurements were recorded. In fact the 10 or so devices studied were grouped into two categories, one behaved as thick cylinders and the other equally populous group responded as if only the outer shell contributed to K_T. As with the 'work hardening' itself, there is no satisfactory explanation of this differentiation between the two groups of samples.

3.2.3. Stick-slip: carbon and WS_2 nanotubes. Yet another mode of response appears in experiments on WS_2 multi-wall nanotubes. WS_2, like graphite, is a commercial lubricant, and so one might expect rather similar behavior [87]. In contrast to the trend in the carbon MWNT, these structures appear to twist as a unit up to some critical value of strain at which point the shells begin to slip relative to each other. The shells then stick together again as the paddle is deflected further until another slip releases some of the strain energy. The difference between the WS_2 results and the carbon MWNT results may be due largely to the different levels of corrugation in the potential energy of one shell that results from the neighboring shells. A model of the competition between torsional strain energy and the van der Waals interaction between the shells was used to explain the stick-slip events with some success in predicting (e.g.) the critical strain angles as a function of the nanotube diameter. These results offer a significant contrast to the MWNT results discussed above. In the MWNT experiments, there was no evidence of stick-slip behavior. Stick-slip has been observed in telescoping motion in MWNT [88, 89]. Apparently the 'corrugation' forces that result from commensuration are larger in WS_2 than in graphene-based nanotubes.
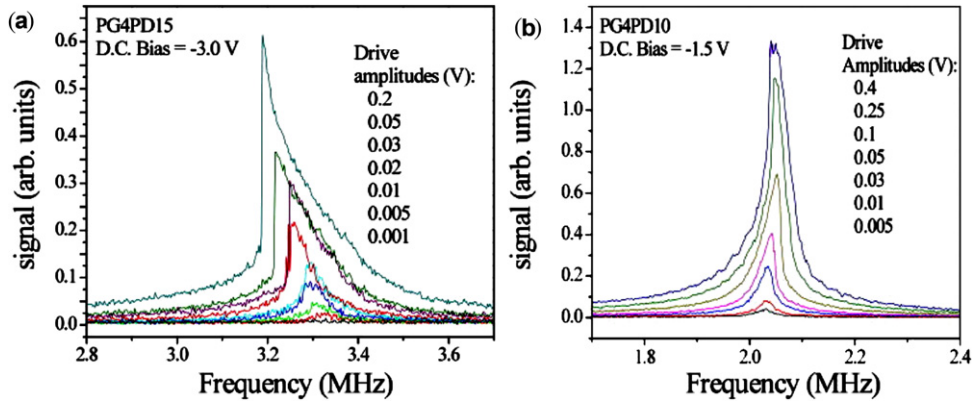
Figure 10. Resonance shape versus drive amplitude for two different paddle oscillators, showing (*a*) hysteretic and (*b*) non-hysteretic behavior. After [68].

3.3. SWNT

Although more recent historically than the experiments on MWNT, the experiments on SWNT are simpler to interpret and to explain. Three groups have performed experiments each in their own particular style and device configuration. AFM has been employed to deflect metal paddles mounted on freely suspended SWNT. Both the force required to deflect the paddle (and the torque to twist the SWNT) and the resistance of the SWNT were measured [20]. In other experiments the deflection was induced electrostatically [90–92], and the forces and torques were modeled [91, 92] through self-consistent finite element solutions for the electrostatic response of the SWNT, paddle and anchors. Paddle oscillators built on SWNT have been driven into resonance by oscillating external electric fields, and the resonance peak detected through changes in the SWNT resistance [86].

3.3.1. Quasi-static torsion and mechanical modulus revisited.
Static and quasi-static torque on SWNT samples has been applied through electrostatic forces by two groups [90, 91, 93]. The first experiment and the last were performed inside TEMs so that detailed structural information could be obtained under strain. Mechanical response was measured and the inferred torsion moduli were compared with theoretical models.

To infer the torque and, through measurements of the strain, the modulus, these authors [91] modeled the electrostatic force in finite element calculations based on self-consistent solution of Poisson's equation. While somewhat indirect, this method allows for exquisite control of the amount of torque. Examples of experimental images and the models used by one group appear in figure 11. The torque on each face can be calculated within the modeled electric field environment and representative torque calculations are included in the figure. The torque on each face is

$$T = \frac{1}{\varepsilon_0} \int_{\text{surface}} dA \, \sigma^2 \vec{r} \times \hat{n}, \qquad (3.5)$$

where the integral is over the surface areas with normal unit vectors $\hat{n}$ and (self-consistent) charge densities $\sigma(\vec{r})$.

The response to the torque is limited by the torsion modulus in the two strands of the same SWNT linking the paddle to the anchors. These two springs act in parallel and
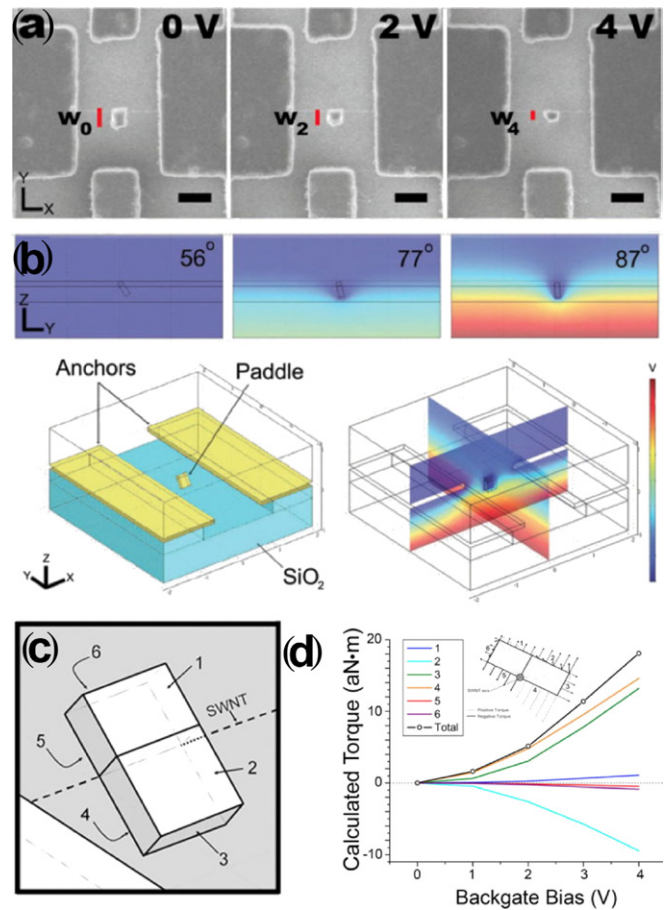
Figure 11. (*a*) Plan-view images of the deflection of a paddle mounted on a SWNT for increasing voltage on the back gate. The red line indicates the projected width *w* (scale bar = 500 nm). (*b*) Finite element models of electric field along symmetry planes of the model of the experiment. The color scale ranges from 0 to 4 V. (*c*) Torques on each face of the cube as calculated from the finite element solutions for electric fields. Adapted with permission from [91]. Copyright 2006 American Physical Society.

one can infer a torsion (shear) modulus of [92]

$$G = \frac{l_1 l_2}{2\pi t r^3 (l_1 + l_2)} \frac{T}{\phi} \qquad (3.6)$$

from a SWNT deflected through an angle ϕ, with l_i being the lengths of the SWNT segments, t and r being the thickness

and radius of the SWNT shell, respectively. In this early experiment [91], the value of r was difficult to pin down accurately in SEM or AFM measurements. The thickness of the shell was simply taken to be the interlayer graphite spacing 0.34 nm. Inferred moduli from six different devices averaged around 2.5 TPa, which is approximately five times larger than predicted in theoretical models [35, 94].

At about the same time, another group [20] applied the torque with an AFM tip. Although their principal focus was to measure the electromechanical response, they also measured the moduli of their SWNT from topography measurements (as opposed to the torsion response described above) and found values much closer to the theoretical predictions.

In contrast to the unexpected results from experiments on the MWNT, the quasi-static deflections of the paddles built on SWNT show no evidence of change with history, and hence none of the 'work hardening'. This fact in itself suggests that the hysteresis seen in the MWNT is probably a result of the coupling of shells in those nanotubes. The methods of sample fabrication were the same for the SWNT experiments as for the MWNT experiments, so any artifact or explanation related to the processing or anchoring of the nanotubes should apply to both sets of devices.

4. CNT torsional electromechanics

4.1. Theoretical understanding

We begin our discussion of CNT torsional electromechanics with a brief review of the current theoretical understanding of the system. Here, we will describe first the effect of torsional strain on CNT band gap and then how changes in band structure are manifest in measured transport properties.

4.1.1. Effects of mechanical strain on band gap. Under torsional strain the effective chiral angle of the nanotube continuously changes. As the electronic properties near the Fermi level are sensitive to the chirality, a strong electromechanical response is expected. There have been several theoretical studies [83, 95–101] on the variation of band gap due to mechanical deformations. Heyd *et al* [102] investigated the effect of uniaxial stress on the electronic density of states using a semi-empirical tight-binding method, and found a linear dependence of the band gap on the stress for zigzag tubes. Kane and Mele [103] predicted the opening of a band gap in armchair tubes under torsion. Yang *et al* [104] showed that under uniaxial or torsional strain, the band gap variation of a zigzag and armchair SWNT is the largest, and is independent of diameter. Using a tight-binding model, Yang and Han [105] derived an analytical expression of the intrinsic band gap change under small strains:

$$\Delta E_{\mathrm{g}} = sgn(2p+1)3t_0[(1+\nu)\sigma \cos 3\theta + \gamma \sin 3\theta], \quad (4.1)$$

where ν is the Poisson ratio, $\sigma = \Delta l/l$ and $\gamma = (\Delta \phi r)/l$ are the uniaxial and the torsional strain, and θ is the tube chiral angle. From the equation it can be seen that for zigzag tubes ($\theta = 0$) the band gap is insensitive to the torsional strain, while for armchair tubes ($\theta = \pi/6$) the gap is insensitive to
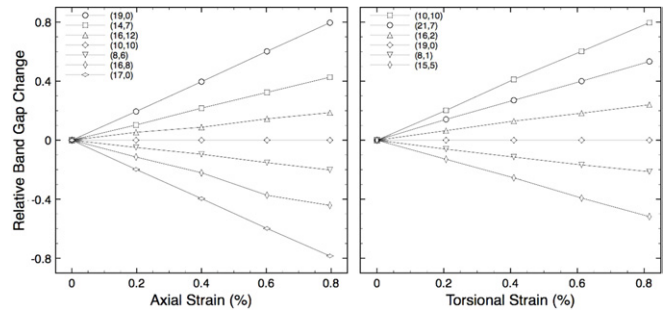
Figure 12. Band gap change of SWNTs under uniaxial and torsional strains. Notice the linear variation of the band gap with the strain and its dependence on the chiral indices. After [105].

the uniaxial strain (see figure 12). The change of band gap under the strain implies possible metal–insulator transitions for all nanotubes. The linear dependence of the band gap on the strain is due to the linear band dispersion of the graphene near the Fermi level. Because the variation of energy levels with the strain is different for different sub-bands, at certain strain the energy levels of sub-bands cross over, thus the band gap as a function of the torsional strain exhibits periodic behavior for large strain [20]. This oscillation of the band gap leads to the periodic metal–semiconductor transitions [96, 98, 106, 107], examples of which are illustrated in figure 13. It is worth mentioning that the band gap of a SWNT also undergoes periodic oscillation with a magnetic field applied along the tube axis, due to the change in effective chirality from the presence of Aharonov–Bohm phase [95, 97]. This can provide another method to observe the effect on the band gap variation with strain [99, 101].

Assuming weak interaction between shells, the variation of band gap with strain in MWNT may be understood in terms of independent SWNT, at least to the leading order.

4.1.2. Transport properties of CNTs subject to strain. If a nanotube of finite length is connected with the metallic probes in perfect ohmic contacts, the conduction is length independent and only determined by the number of available quantum channels and quantum conductance per channel [108] $G_0 = 2e^2/h$. For each SWNT there are two energy sub-bands across the Fermi level, thus metallic SWNTs have the quantized resistance of $R_0 = 1/2G_0 = 6.5 \,\mathrm{k}\Omega$ in the ballistic limit [109]. For semiconducting CNTs, the conductance at low temperature is determined by thermal activation of carriers [110], consequently the low-bias resistance of semiconducting CNT can be expressed as [111, 112]

$$R_{\mathrm{CNT}} = \frac{1}{|t|^2} \frac{R_0}{2} \left[1 + \exp\left(\frac{E_{\mathrm{g}} + \Delta E_{\mathrm{g}}}{kT} \right) \right], \quad (4.2)$$

where $|t|^2$ is the transmission probability across the band gap. Given the proper determination of the metal electrodes with large work function to suppress Schottky barriers, reliable ohmic contacts to both metallic and semiconducting SWNTs can be achieved [113, 114], and the effects of contact resistance can be minimized.

For most experiments the torsional strain is applied by a metal paddle attached to a suspended nanotube, which is
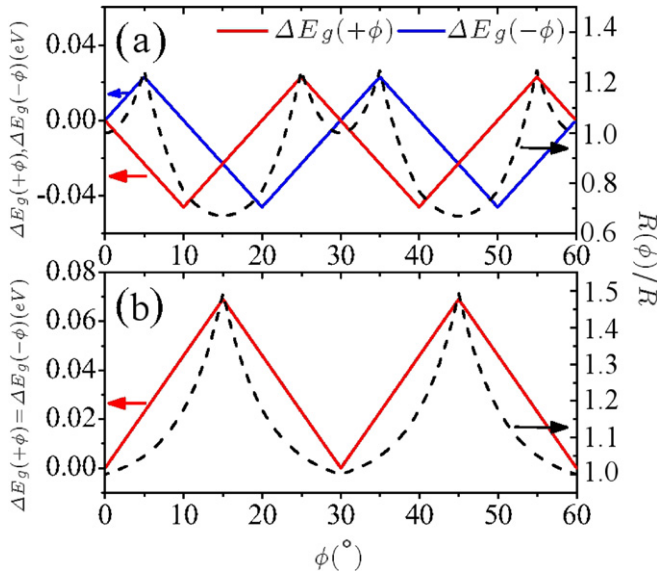
Figure 13. Examples of the calculated band gap (solid lines) and resistance (dashed lines) oscillations with torsional strain. In the case of semiconducting tube (*a*) the band gap in the two sides of the paddle varies in the opposite directions as the torsion is opposite. The resistance always increases initially as it is dominated by the weakest link. For metallic nanotubes (*b*), the band gap variation is independent of the sign of the torsion angle ϕ. The period of oscillations scales as the inverse square of nanotube diameter. Reproduced with permission from [83]. Copyright 2008 American Physical Society.

twisted along with the paddle by an electric field or by an AFM cantilever [22, 23, 91, 93, 111, 112, 115–117], with the two ends of the nanotube anchored. Under torsion, the two halves of the nanotube are twisted in opposite directions by $+\phi$ and $-\phi$. Assuming that the lengths of exposed CNT are equal on either side, the total resistance R_T is then given by

$$R_T = R_C + R_{CNT}(+\phi) + R_{CNT}(-\phi), \qquad (4.3)$$

where R_C is the contact resistance with the metal electrodes. In the case of a metallic SWNT device, identical band gaps are opened on both sides, and the total resistances would increase. But for a semiconducting SWNT device, the band gap of either segment can increase or decrease depending on its intrinsic chirality. The net effect on the total resistance change can be more complex. Examples of the variation of resistance with deflection angle for both metallic and semiconducting tubes are shown figure 13.

For MWNT, if there is good electric coupling between the shells, the conductance is the superposition of individual inner tubes; that is, $\sum_i G_i$ where G_i is the conductance of the ith shell [19, 118, 119]. The greatest inter-shell electric coupling occurs when all shells have the same chirality. For typical MWNT, it is generally agreed that neighboring shells are incommensurate (see section 5 below), so current moving along an individual shell is efficiently insulated from others. Therefore, in the absence of defects linking the shells, the electromechanical response of a MWNT under torsional strain may be expected to be similar to that of the outermost shell alone [120–124].

4.2. Non-torsional nanotube deformations

Previous devices have exploited the electromechanical effect of non-torsional CNT deformations. For instance, studies of armchair [98] and metallic zigzag [107] CNT have shown that a band gap can be created or changed by radial deformation, but the size of the effect is very sensitive to the details of the deformation, which is characterized by d_{tb}, the distance between the top and bottom of the deformed CNT. This type of measurement was first realized experimentally by Gómez-Navarro *et al* [125], who observed fluctuations in low-bias transport through a SWNT as a function of d_{tb}.

Similarly, axial deformations have been studied by strain applied locally and perpendicular to the CNT axis with an AFM tip [115, 125, 126]. For example, Tombler *et al* [115] suspended a section of a CNT over a trench in a SiO$_2$ substrate, and metal contacts anchoring either end served as electrical leads. As the AFM tip deformed the CNT, the suspended section was stretched approximately uniaxially and at the point of contact with the AFM tip there was significant radial deformation. The measured conductance changed reversibly by two orders of magnitude, indicating the emergence of a band gap.

Later, the use of the scanning probe as a means by which to apply axial strain was extended. Minot *et al* [112] used a metalized AFM tip as a gate electrode in order to characterize the transport characteristics of a stretched SWNT. To relate the measured resistance of a tube to its band structure, thermal excitations across the gap were considered and contributions of tunneling were neglected. They found a distinct correlation between applied axial strain and transport properties and, importantly, observed different responses from different SWNTs, in line with theoretical works described above.

4.3. Special fabrication considerations for transport measurements

The initial photolithography pattern used for electrical measurements must be composed of separate electrodes so that opposing ends of the target nanotube can be contacted independently. Care must be taken in designing electrical measurement schemes—especially if nanotubes bridge multiple electrodes prior to fabrication. For liquid-deposited MWNT, this is generally not an issue due to their length (∼1 μm), but for CVD-grown SWNT and DWNT, very long (up to 1 mm) nanotubes are routinely produced. A simple solution to remove inconvenient contacts is to ramp the voltage (from 0 to 100 V) between each set of electrodes. This removes highly localized sections of nanotubes oxidatively [127] (see, for example, the small gaps in the SWNT in figure 8).

4.4. MWNT torsional electromechanics

The first study of torsional strain effects on transport was performed in 2006 [20] with a torsional element fabricated on an individual MWNT. Actuation was performed directly with a scanning probe in a fashion similar to previous work [22].
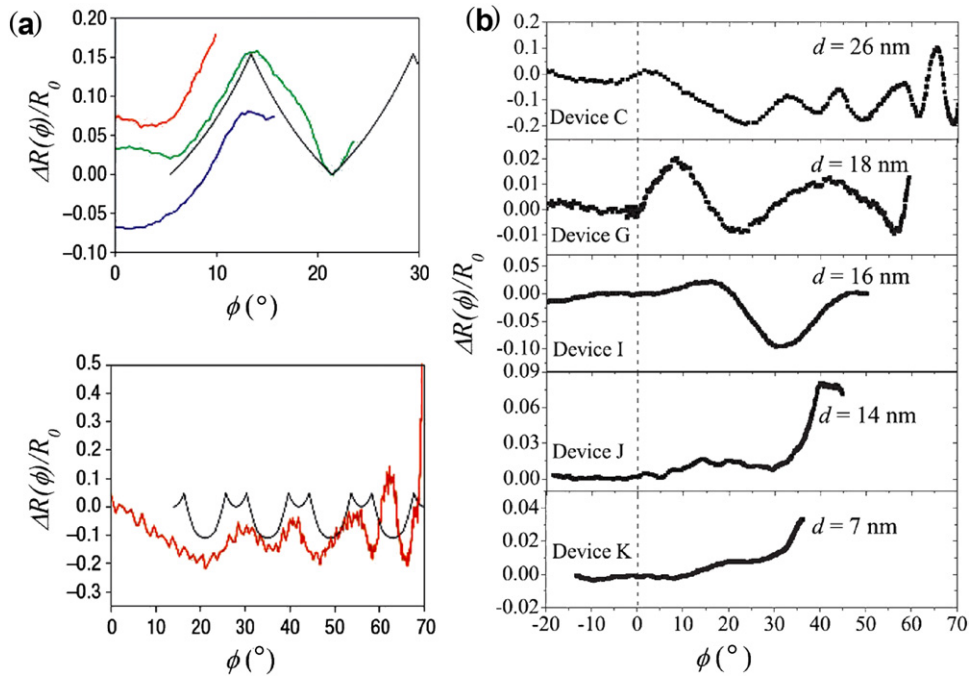
Figure 14. (*a*) Oscillations observed in MWNT resistance (normalized to original resistance R_0) through torsional deflection ϕ. (*b*) Behavior of several MWNT with different outer diameters (indicated), showing periodicity. After [20] and reproduced with permission from [83]. Copyright 2008 American Physical Society.

Here, however, low-bias (10 mV) nanotube resistance was monitored during the actuation. In the resulting measurements, an oscillatory behavior was seen in the transport properties as the probe tip exerted increasing torsional strain on the MWNT (figure 14(*a*)). Total loss of conductance was also recorded at large deflection, demonstrating that the transport measurement was indeed conducted through the nanotube. Later, experiments by the same group studied the response of several different MWNTs with different outer diameters to torsional strain [83] (figure 14(*b*)). These more extensive measurements revealed that the period of the resistance oscillations varied with the inverse square of nanotube diameter.

The observed dependence was attributed to the movement of Fermi points through allowable *k* states. Since the spacing of these states narrows as the nanotube diameter increases, thicker MWNT were able to pass through a greater number for the same amount of torsional deflection. These results ultimately support a predominantly *intra*shell electromechanical effect, and suggest that transport is only through the outermost shell of the MWNT. This indicates that MWNTs are, in fact, composed of coaxial shells of graphitic carbon that act independently from one another—at least electronically. This measurement technique may also represent a route toward further exploration of the 'work-hardening' effect discussed previously, wherein inter-shell coupling is thought to increase over multiple torsional deflections. So far, only a limited number (~3) of repeated actuations have been explored with the electromechanical method, while the associated mechanical stiffening became appreciable over hundreds of deflections.

4.5. SWNT torsional electromechanics

Another form of the torsional device was fabricated on CVD-grown SWNT. The shear modulus of SWNT [35] is much lower than the MWNT, so measurement of torsional strain with a scanning probe tip was not convenient due to the limited force resolution of the technique. Therefore, these devices were actuated with a dc bias applied to the backgate electrode (see also sections 3.2.2 and 3.3.1) while SWNT transport was monitored [117].

Transport measurements of SWNT devices prior to the final etch step showed little to no dependence on applied backgate voltage (figure 15, red) due to the large oxide thickness. After etching, however, nanotube resistance changed with the backgate voltage (figure 16, blue), and therefore with paddle deflection. After transport measurements, a series of scanning electron micrographs were taken of a given device from above over the same range of backgate voltages, both positive and negative. Measurement of the projected width of the paddle allowed for a measure of its deflection angle at the given gate value (figure 15, open circles). The symmetric dependence on backgate voltage was consistent with a torsional strain effect, since the application of either positive or negative voltage to the backgate results the same torsional strain in the SWNT. Importantly, some devices demonstrated an *increase* in source–drain resistance when deflected while others demonstrated a *decrease* (figure 16).

In principle, a possible explanation for the measured transport change is that the metal–SWNT contact at the anchor electrodes is altered by electrostatic deflection of the nanotube. Those portions of the SWNT are buried under the deposited metal pads, however, so electrostatic attraction is capable only of deflecting the tube toward the substrate and away from the
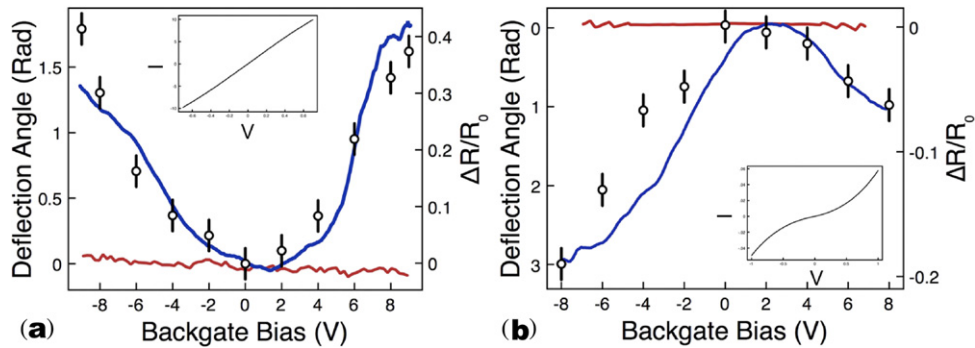
Figure 15. SWNT differential resistance dependence on applied backgate voltage both before (red) and after (blue) device suspension. The nanotube in (*a*) showed a resistance increase while the nanotube in (*b*) showed a resistance decrease. Open circles represent torsional deflection angle as measured from projected width (see figure 11). Insets show *I*−*V* characteristics measured before device suspension. Adapted with permission from [117]. Copyright 2007 Nature Publishing Group.
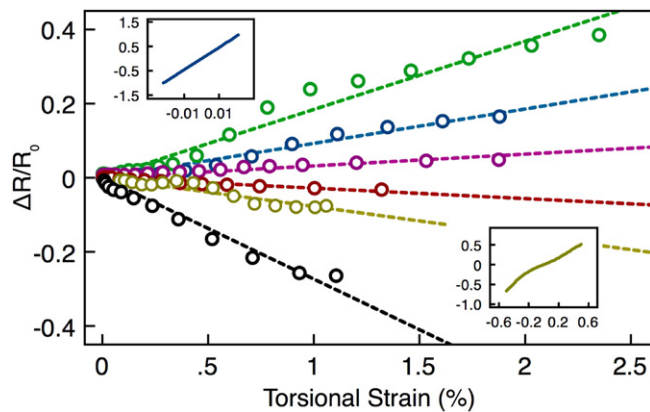
Figure 16. Dependence of SWNT differential resistance on torsional strain for six different devices demonstrating the range of reactions observed. Insets: examples of *I*−*V* characteristics for two devices (color indicated). Adapted with permission from [117]. Copyright 2007 Nature Publishing Group.

contact. While this could explain an increase in measured resistance, the observed decrease in resistance for some devices cannot be accounted for. Additionally, devices fabricated with long exposed sections of SWNT did not reveal measureable resistance changes at all. While these devices would still be affected by possible changes to the nanotube contact, the strain applied to the tube for the same torsional deflection would be much less.

SWNT differential resistance versus strain γ could be determined through the relation $\gamma = \mathrm{d}l/2\phi$, where d is the nanotube diameter, l is the exposed nanotube length (measured from SEM images), and ϕ is the deflection angle. Nanotube diameter was again difficult to determine, so the mean SWNT radius (0.49 nm) from the measured distribution (figure 7(*a*)) was used. Figure 16 shows the measured response for six different SWNTs. In accordance with theory, the various observed reactions were associated with changes in the nanotube band gap. All nanotubes with decreasing resistance showed nonlinearity in their *I*−*V* characteristics, while those with increasing resistance varied in their linearity (figure 16, insets). This result also agrees with the torsional mechanism, as a tube with no initial band gap (i.e. linear current–voltage characteristics) has zero energy gap to start with and so cannot undergo a decrease in the gap.

4.5.1. Resonance oscillations. As with any other spring mass system, it is possible to drive a SWNT paddle oscillator into resonant oscillations if the appropriate frequency of oscillatory force is applied. Detection of the resonance typically was not carried out with light scattering because the paddles were too small to elicit a response. It was also not carried out in situ in a TEM or SEM because the resonant frequencies were in the MHz range and hence far too rapid for TEM imaging. Analysis of image 'motion blurring' can be used to detect motion [12, 86, 90], but a more refined method (that deposits no amorphous carbon onto the sample) is to use the electromechanical response of the SWNT as a sensing method [20, 86]. As the actuation voltage approaches the resonance frequency, the amplitude of device oscillation increases as well, causing the paddle to reside at a higher average deflection angle during the measurement. This manifests as a measurable peak in the source–drain resistance that is highly localized in frequency space. Instead of apparent quality factors $Q = \Delta\omega/\omega_0 = 10$, where ω_0 is the resonance frequency, the values of Q easily range up to several hundred with this self-contained measurement technique. Representative data are in figure 17 where the piezoresistance sensing method shows clear superiority in quality factor. Further experiments on drive amplitude dependence are in qualitative agreement with theoretical estimates of the electromechanical response and with earlier experiments [20, 86, 111, 112, 116].

5. Transmission electron microscopy studies of CNT torsion

Both SWNT and MWNT were first observed and identified in transmission electron microscopes [1, 2, 128]. Transmission electron microscopy techniques, including imaging, electron diffraction, and *in situ* manipulation when nanotube device is actuated, have become more important when the data of deformation of CNT are sought at the atomic level. TEM offers a unique experimental capability to study the properties of single CNT-based device with high precision. It provides additional, unique and complimentary capabilities to the other techniques described in other sections of this paper. In particular, TEM techniques can permit high-precision measurement of the number of shells, chirality of

14

each shell, and twisting of each shell of the CNT under torsional strain *in situ*. In order to obtain and examine experimental measurement of actuated single CNT NEMS devices, we have developed and applied electron imaging and electron diffraction methods *in situ*. Methods and results on (1) the determination of chirality of each shell of CNTs, (2) determination of twist angle by electron diffraction, (3) fabrication of TEM-suitable single CNTs NEMS device, (4) measurement of the inter-shell friction and the shear modulus of CNTs, and (5) measurement of handedness of single CNTs are reviewed in this section.

5.1. Determination of chirality of CNTs

As described in section 1, the atomic structure of a SWNT can be well described by its chiral indices (u, v). Once these indices are defined, their numerical values can be determined using nano-beam electron diffraction, a technique that enables the determination of chiral indices of each shell in a MWNT. As detailed in an earlier article by Qin [129], the chiral indices can be derived from the electron diffraction pattern by the following two complementary methods: (i) using the Bessel function and (ii) using the line spacing ratios.

5.1.1. Bessel function method. When an electron diffraction pattern is formed from a straight segment of a SWNT, the total electron scattering amplitude can be expressed analytically as [132–130]

$$F(R, \Phi, l) = \frac{f}{c} \sum_{n=-\infty}^{n=+\infty} \exp\left[in\left(\Phi + \frac{\pi}{2}\right)\right]$$
$$\times \int_0^c \int_0^{2\pi} \int_0^\infty V(r, \phi, z) J_n(2\pi r R)$$
$$\times \exp\left[i\left(-n\phi + \frac{2\pi l z}{c}\right)\right] r \, dr \, d\phi \, dz, \quad (5.1)$$

where f is the atomic scattering amplitude of carbon atom for electrons, c is the axial periodicity of the CNT, $V(r, \phi, z)$ is the Coulomb potential of the CNT, $J_n(x)$ is the Bessel function of order n, and (r, ϕ, z) and $(R, \Phi, Z = l/c)$ are the cylindrical coordinates of the CNT in real space and reciprocal space, respectively. If the distribution of concrete carbon atom positions (r, ϕ_j, z_j) on the cylindrical surface of radius r is included, the total scattering amplitude then becomes

$$F(R, \Phi, l) = \sum_{j=1}^{N} \sum_{n=-\infty}^{n=+\infty} f J_n(2\pi r R) \exp\left[in\left(\Phi + \frac{\pi}{2}\right)\right]$$
$$\times \exp\left[i\left(-n\phi_j + \frac{2\pi l z_j}{c}\right)\right], \quad (5.2)$$

where N is the total number of carbon atoms within a length of axial periodicity c.

The experimentally acquired electron intensity distribution is then

$$I(R, \Phi, l) = |F(R, \Phi, l|^2. \quad (5.3)$$

Although the expression of the electron scattering intensity on a particular layer line of index l involves multiple Bessel functions $J_n(2\pi r R)$ of different orders n, it turns out, fortunately, that only one order of the Bessel functions for each layer line of index l dominates. The order of the dominant
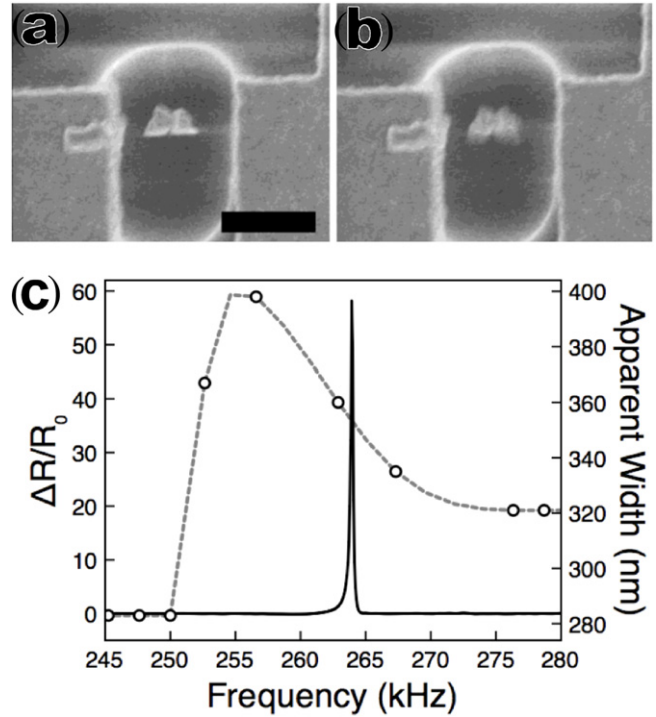
Figure 17. SEM images recorded for drive frequencies (*a*) 245 kHz and (*b*) 257 kHz. Scale bar represents 500 nm. (*c*) Comparison of resonance shape measured by the SWNT piezoresistance (solid line) to added apparent blurring of the image (open circles). Adapted with permission from [86]. Copyright 2008 American Chemical Society.

Bessel function for layer line l (see figure 18) is related to the chiral indices (u, v) by the equations [133–137]

$$I_{l1}(R) \propto |J_v(2\pi r R)|^2 \quad (5.4)$$
$$I_{l2}(R) \propto |J_{-u}(2\pi r R)|^2 = |J_u(2\pi r R)|^2 \quad (5.5)$$
$$I_{l3}(R) \propto |J_{u+v}(2\pi r R)|^2 \quad (5.6)$$

and

$$I_{l4}(R) \propto \left|J_{-(u-v)}(2\pi r R)\right|^2 = |J_{u-v}(2\pi r R)|^2. \quad (5.7)$$

Since the order of a Bessel function $J_n(X)$ can be determined from its intensity distribution, for example, the order n can be obtained by examining the ratio of the positions of the first peak and the second peak X_1/X_2, which is unique to each order of Bessel function, the respective chiral indices can be obtained from layer lines l_1 and l_2. Equations (5.6) and (5.7) can be used as supplementary relationships to improve the accuracy of the determination from the method.

5.1.2. Layer-line ratio method. An alternative method to obtain the chiral indices (u, v) is to use the ratio of the layer-line spacing D_l. In this method, the chiral indices (u, v) are derived from the geometry of the diffraction pattern. It can be shown that, the ratio of the chiral indices v/u can be expressed by the principal layer-line spacings as [138–140]

$$\frac{v}{u} = \frac{2D_2 - D_1}{2D_1 - D_2} = \frac{2D_2/D_1 - 1}{2 - D_2/D_1}, \quad (5.8)$$

and in many cases, the chiral indices (u, v) can be obtained unambiguously from the ratio of line spacings D_2/D_1.
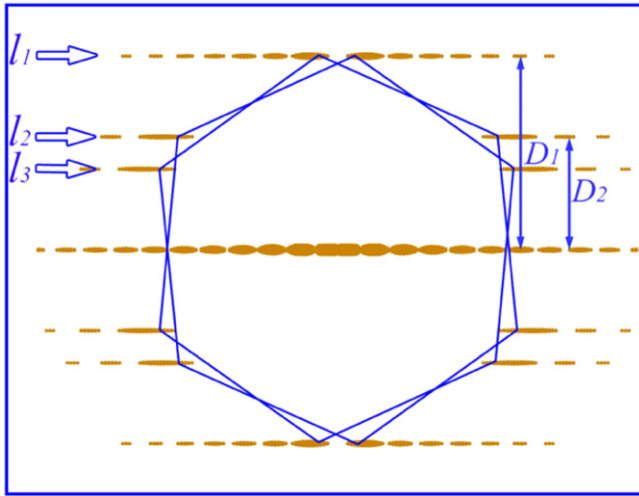
Figure 18. Schematic diffraction pattern of a SWNT. The principal layer lines are labeled l_1, l_2 and l_3 and their corresponding line spacings relative to the equatorial line are D_1, D_2 and D_3 (not indicated in the figure). Reproduced with permission from [134]. Copyright 2005 Elsevier.

Figure 19. Zones separated by the reflection layer lines between zigzag and armchair nanotubes in reciprocal space. Layer lines l_1, l_2 and l_3 will always be confined in the zones L_1, L_2 and L_3, respectively. After [141].

Convenient tables relating the chiral indices (u, v) and the layer-line ratios have been made available in the literature from tabulated v/u [129, 140].

5.1.3. MWNT. As illustrated in figure 18, if the nanotube is non-helical, there are three principal layer lines above the equatorial line and three below it. Therefore, there would be usually $3m$ pairs of principal layer lines on an electron diffraction pattern of CNTs with m shells. When two or more shells have the same helicity, the diffraction patterns due to these shells would overlap with each other. In addition, if there is a non-helical shell in the MWNT, the number of principal layers would also be reduced. These factors need be considered when one analyzes the diffraction patterns.

When the number of shells becomes larger, the number of layer lines also increases quickly and it could be rather challenging to sort the reflection layer lines. To assist the grouping and assignment of the layer lines in terms of the tubule shells that cause the corresponding layer lines in the electron diffraction pattern, we have developed a zoning scheme as illustrated in figure 19 [141]. There will be $3m$ layer lines in each zone. The top-most layer line in zone L_1, the bottom-most layer line in zone L_2, and the top-most layer line in zone L_3, will be due to the same shell. Similarly, the second layer line from the top in zone L_1, the second layer line from the bottom in zone L_2, and the second layer line from the top in zone L_3, will be due to the same shell. Analogously, all layer lines in the diffraction pattern can be sorted out and grouped systematically with ease.

Once the layer lines are sorted, the chiral indices of each shell can be obtained using the methods described in sections 5.1.1 and 5.1.2.

5.2. Determination of twist angle and handedness

When a CNT is twisted about its axis, as illustrated in figure 20, if the twist angle is small, we can assume that all carbon hexagons are deformed uniformly. When the twist angle is smaller than the threshold angle at which buckling would occur, the deformation of the graphene is illustrated in figure 20(*c*). If the chiral indices of the CNT are (u, v) and the CNT is twisted uniformly by an angle of $(u + 2v)\phi/(uM)$ about its axis, where M is the maximum common divisor of $(2u + v)$ and $(u + 2v)$, the pitch length of the twisted helix will become $C' = C/(1 + \phi/2\pi)$. On the corresponding electron diffraction pattern, the twisting angle ● can be related to the layer-line spacings in the equation [142]
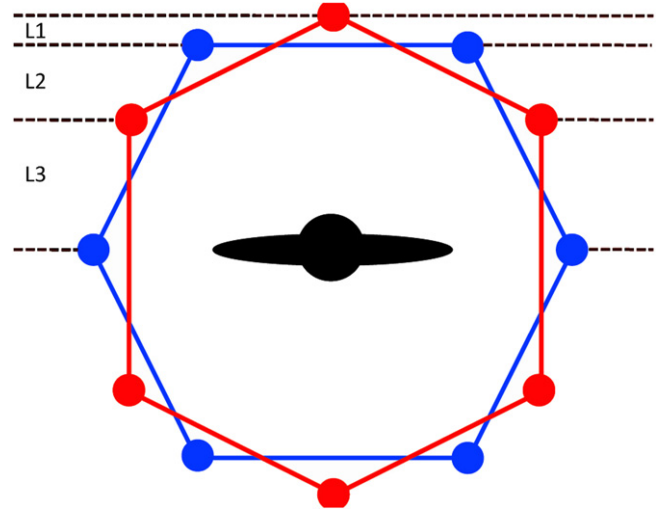
$$\frac{\phi}{2\pi} = \frac{(2u + v)/(u + 2v) - D_1/D_2}{D_1/D_2 + v/u},\qquad(5.9)$$

where D_1 and D_2 are the layer-line spacings of the twisted CNT. Therefore, for a CNT of known chiral indices (u, v), when it is twisted under uniform torsional strain, the twist angle ϕ can be obtained from its electron diffraction patterns acquired under torsion. These results are useful for determining the handedness and twist angle of CNTs.

Figure 21 shows how the layer lines move when the CNT (22,2) is twisted. When the CNT is twisted counterclockwise ($\phi = -1.2°$ nm^{-1}), layer line l_1 moves away from equatorial line and layer lines l_2 and l_3 move toward each other. When the CNT is twisted clockwise ($\phi = +1.2°$ nm^{-1}), layer line l_1 moves toward the equatorial line and layer lines l_2 and l_3 move away from each other. These detectable phenomena will be used experimentally to examine the absolute direction of twisting to obtain the handedness of the nanotube.

5.3. Special fabrication considerations for in situ TEM

To fabricate TEM-suitable samples, the CNT must be exposed to the electron beam within a through-hole across which the individual CNT is suspended. In fabricating the single CNT NEMS devices, we applied different CVD procedures for obtaining SWNT and DWNT using different CVD procedures
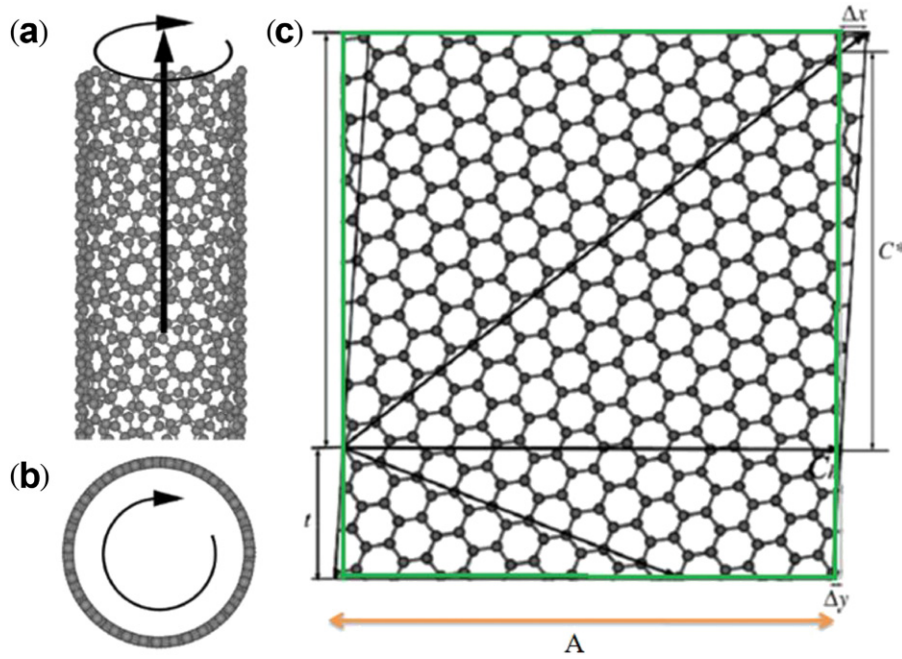
Figure 20. (*a*) Schematic illustrating clockwise twisting of a CNT about its axis in side-view. (*b*) Viewed end-on of the same situation. (*c*) Radial projection of a twisted CNT. Green-lined rectangle and dark-lined parallelepiped are the graphene cut before and after twisting. Reproduced with permission from [142]. Copyright 2005 Elsevier.
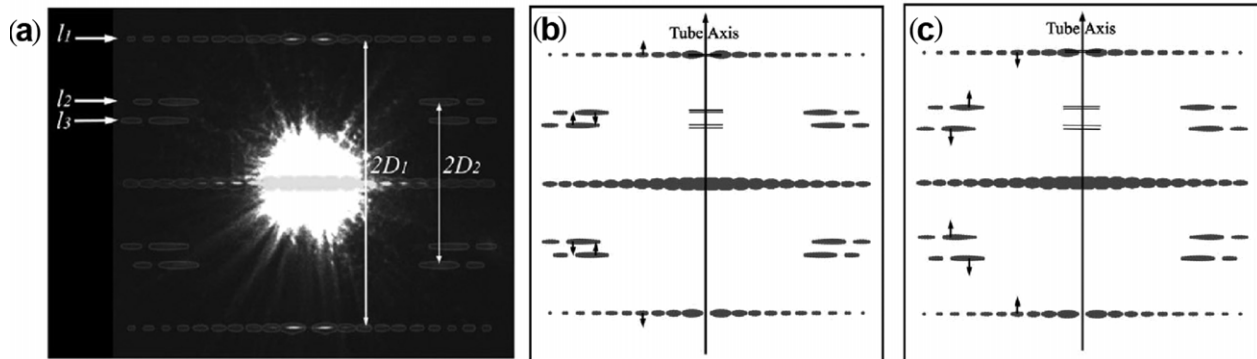
Figure 21. Changes of the geometry of electron diffraction pattern when a CNT is twisted uniformly. (*a*) Experimental electron diffraction pattern of CNT (22,2). Simulated pattern is also plotted on the experimental pattern. (*b*) Simulated electron diffraction pattern of CNT (22,2) twisted counterclockwise. (*c*) Simulated electron diffraction pattern of CNT (22,2) twisted clockwise. Arrows in (*b*) and (*c*) indicate directions of shifting of the later lines relative to untwisted CNT. Reproduced with permission from [142]. Copyright 2005 Elsevier.

[143–145]. To obtain a through-hole in the substrate on which CNTs are grown, electrodes and interconnects are fabricated, critical point dry etching as well as focused-ion beam (FIB) were utilized to obtain TEM-ready device illustrated in figure 22 [145]. In a finished TEM-suitable device, a single CNT is suspended across an open window, as shown in the TEM image given in figure 22(*d*).

When a bias voltage is applied between the gate electrode and the metal paddle, the nanotubes will be twisted. In our experiments, we recorded both TEM images and electron diffraction patterns for analysis of the torsional deformation of the nanotubes.

5.4. Measurement of shear modulus and inter-shell friction

The shear modulus of a CNT is related to torsional device characteristics through equation (3.2), where $K_T = T/\phi$. In

in situ experiments, the deflection angle ϕ and the lengths l_1 and l_2 were measured directly from real space images, and the net torque was obtained using numerical simulations from known geometry of the device as discussed above. For a DWNT, the shear moduli of the outer shell and the inner shell were measured to be 0.50 ± 0.01 TPa and 0.41 ± 0.05 TPa, respectively [146]. These values are in good agreement with the theoretical predictions [147].

The inter-shell friction in a DWNT is obtained by calculating the work done by the inter-shell friction when torsion-induced angular displacement takes place. The work done by friction W_f satisfies the following equation:

$$W_f = W_T - \Delta E_S - \Delta E_W, \qquad (5.10)$$

where W_T is the work the external torque, ΔE_S is the change in strain energy of the nanotube, and ΔE_W is the change in
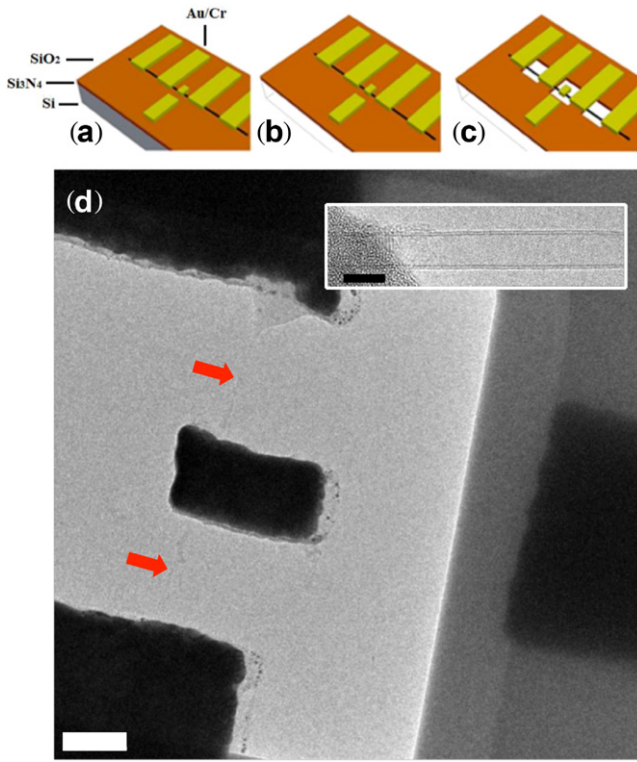
Figure 22. Flow-chart of procedures to fabricate TEM-suitable device. (*a*) Deposition of electrodes on selected CNT. (*b*) Removal bulk of silicon from the back side by HNA etching. (*c*) Further etching using FIB and BHF to produce through-holes where CNT is exposed. (*d*) TEM image of a finished device with one fully suspended CNT and a paddle on it (scale bar 200 nm). Red arrows indicate CNT position. Inset shows a typical DWNT employed in these devices (scale bar 5 nm). After [145].

Figure 23. Relative strain between the inner and outer walls of a DWNT. Reproduced with permission from [146]. Copyright 2011 American Physical Society.

From this result it was possible to obtain the force of friction $F = 2.6 \pm 1.0$ fN/atom between the shells [93]. The measured friction is slightly greater than that measured from another experiment where no detailed structural characterization was performed [89]. In the latter experiment a MWNT was anchored at one end and one of the inner shells was attached to a probe, and the probe enforced a telescoping motion, which self-selects the weakest friction. Another difference is that in the telescoping motion the contact area is shrinking continually during the measurement, which again biases toward a low value of friction.

5.5. Measurement of handedness of CNT

CNTs are enantiomeric. When a CNT is twisted about its axis, the pitch of the helix will become smaller or larger depending on the handedness of the nanotube relative to the sense of the twist as discussed in section 5.2. Figure 21 illustrates the effects in the diffraction pattern. By taking advantage of this phenomenon we can measure the handedness of CNTs [90, 142, 148, 149]. In our experiments, SWNTs of both left-handed and right-handed were observed. In MWNT, no evident correlation in handedness of the tubule shells was observed in our study. Within a MWNT, both left-handedness and right-handedness were observed in its constituent shells [145].

6. Future directions and conclusions

While measurements on torsional devices have already revealed much about the basic mechanics and electromechanics of CNT, there is a wide array of information that the system may be able to address in future studies. In a general sense, the torsional device platform provides a means by which to investigate friction at the nanometer scale. As pristine graphitic lattices have a well-defined structure, it is reasonable to model their interactions with one another.

van der Waals energy due to the inter-shell interactions. The average value of kinetic friction for a DWNT of chiral indices (37,18) (diameter $d_i = 3.805$ nm, helicity $\alpha_i = 18.72°$) and (56,2) (diameter $d_o = 4.467$ nm, helicity $\alpha_o = 1.74°$) for the inner and outer shells, respectively, is [146]

$$f_k = (2.1 \pm 0.9) \times 10^{-9}\,\text{N}$$
$$= (2.6 \pm 1.0) \times 10^{-15}\,\text{N/atom}.$$
(5.11)

The average static friction at gate voltages of 40 and 60 V was obtained as [146]

$$f_{S,40\,V} = (2.7 \pm 1.9) \times 10^{-9}\,\text{N}$$
$$= (3.4 \pm 2.2) \times 10^{-15}\,\text{N/atom}$$
(5.12)

and

$$f_{S,60\,V} = (4.3 \pm 2.4) \times 10^{-9}\,\text{N}$$
$$= (5.3 \pm 2.9) \times 10^{-15}\,\text{N/atom}.$$
(5.13)

The measured strain for each shell (see figure 23) allowed for the analysis of torque balances between the two shells. From the inferred change in strain energy—including the effect of changes in the van der Waals coupling between the two shells—the work done by friction could be calculated.

Torsional actuation of DWNT or MWNT puts relative proximal motion of graphitic planes into practice. Direct experimental measurements on such system could expand our understanding of this most basic phenomenon, offering insights into energy loss mechanisms relevant to all mechanical systems.

Focusing specifically on CNT, among the largest unknowns currently is the effect of inter-shell coupling in MWNT. The 'work hardening' effect first observed in scanning probe-based measurements [22] and later supported by resonant oscillation experiments [68] suggests that concentric shells of a MWNT can interact strongly, but that not all do. What is it that determines the level of these interactions? Will the effect only exist with certain combinations of shell chiralities? Or is this phenomenon a result of defects in the graphitic lattice? Torsional experiments—especially chirality-resolved experiments conducted *in situ* in the TEM—seem poised to address these questions.

The device platform itself is positioned as a general tool for elucidating the torsional mechanical and electromechanical properties of nanotubes and nanowires in addition to CNT. Studies on WS_2 nanotubes [87] demonstrate this potential, but experiments are limited only by the methods used, that is, the fabrication and suspension techniques must be modified to account for material solubility. There may even be device definition techniques that could permit comparable measurement of polymers and biomolecules.

Alternative device actuation schemes may play an important role in future investigations as well. For example, we foresee that certain strategies could allow for actuation with applied magnetic fields. Emerging techniques for fabrication on flexible substrates [150–152] could offer new mechanisms as well, since actuation of a substrate necessarily imparts force on the supported device. We predict that the axial–torsional coupling [61–64] mentioned earlier in this review could be one way to apply this method to a torsional device. In this way, large-scale mechanical motion could be used to enforce nanometer-scale torsional actuation.

Applications for torsional devices include high-switching speed mirrors and variable resistors. In resonance, the system holds particular potential for biological and chemical mass sensing. While ultrasensitive mass sensors based on CNT have been demonstrated [15, 153, 154] the torsional structure has the advantage of incorporating a localized gold platform, which allows the use of thiol groups for chemical-specific detection. Recent advances in CNT circuits may improve the signal-to-noise ratio of such sensors [155].

In this review, we have presented an overview of experiments and underlying theory of torsional strain in CNT. We have discussed both the torsional mechanical properties and the electrical response to torsional strain in MWNT and SWNT. Experimental investigations have been generally in close agreement with theoretical explanations, demonstrating the robustness of our understanding of the system. We have also reviewed experiments performed *in situ* in a TEM. These studies have exploited the atomic-level analytical capabilities of TEM to monitor directly the effects of torsional strain on *individual* shells of a DWNT, demonstrating how strain is coupled between shells and allowing crystalline handedness

to be determined. In total, the topics reviewed here have revealed much about the microscopic details of nanotube torsion. Continuing investigations promise to answer still more questions and to establish applications for the device platform.

References

[1] Iijima S 1991 Helical microtubules of graphitic carbon *Nature* **354** 56–8

[2] Iijima S and Ichihashi T 1993 Single-shell carbon nanotubes of 1 nm diameter *Nature* **363** 603–5

[3] Wallace P R 1947 The Band Theory of Graphite *Phys. Rev.* **71** 622–34

[4] Mintmire J W, Dunlap B I and White C T 1992 Are fullerene tubules metallic? *Phys. Rev. Lett.* **68** 631–4

[5] Hamada N, Sawada S-I and Oshiyama A 1992 New one-dimensional conductors: graphitic microtubules *Phys. Rev. Lett.* **68** 1579–81

[6] Saito R, Fujita M, Dresselhaus G and Dresselhaus M S 1992 Electronic structure of chiral graphene tubules *Appl. Phys. Lett.* **60** 2204–6

[7] Dresselhaus M S, Dresselhaus G and Eklund P 1996 *Science of Fullerenes and Carbon Nanotubes* (San Diego, CA: Academic)

[8] Odom T W, Huang J-L, Kim P and Lieber C M 1998 Atomic structure and electronic properties of single-walled carbon nanotubes *Nature* **391** 62–4

[9] Blase X, Benedict L X, Shirley E L and Louie S G 1994 Hybridization effects and metallicity in small radius carbon nanotubes *Phys. Rev. Lett.* **72** 1878–81

[10] Kleiner A and Eggert S 2001 Curvature, hybridization, and STM images of carbon nanotubes *Phys. Rev.* B **64** 113402

[11] Schonenberger C, Bachtold A, Strunk C, Salvetat J P and Forro L 1999 Interference and interaction in multi-wall carbon nanotubes *Appl. Phys.* A **69** 283–95

[12] Poncharal P, Wang Z L, Ugarte D and De Heer W A 1999 Electrostatic deflections and electromechanical resonances of carbon nanotubes *Science* **283** 1513–6

[13] Sazonova V *et al* 2004 A tunable carbon nanotube electromechanical oscillator *Nature* **431** 284–7

[14] Chiu H Y, Hung P, Postma H W C and Bockrath M 2008 Atomic-scale mass sensing using carbon nanotube resonators *Nano Lett.* **8** 4342–6

[15] Jensen K, Kim K and Zettl A 2008 An atomic-resolution nanomechanical mass sensor *Nature Nanotechnol.* **3** 533–7

[16] Lassagne B, Garcia-Sanchez D, Aguasca A and Bachtold A 2008 Ultrasensitive mass sensing with a nanotube electromechanical resonator *Nano Lett.* **8** 3735–8

[17] Jensen K, Weldon J, Garcia H and Zettl A 2007 Nanotube radio *Nano Lett.* **7** 3508–11

[18] Evoy S *et al* 1999 Nanofabrication and electrostatic operation of single-crystal silicon paddle oscillators *J. Appl. Phys.* **86** 6072

[19] Bourlon B, Miko C, Forró L, Glattli D C and Bachtold A 2004 Determination of the intershell conductance in multiwalled carbon nanotubes *Phys. Rev. Lett.* **93** 176806

[20] Cohen-Karni T, Segev L, Srur-Lavi O, Cohen S R and Joselevich E 2006 Torsional electromechanical quantum oscillations in carbon nanotubes *Nature Nanotechnol.* **1** 36–41

[21] Fennimore A M *et al* 2003 Rotational actuators based on carbon nanotubes *Nature* **424** 408–10

[22] Williams P A *et al* 2002 Torsional response and stiffening of individual multiwalled carbon nanotubes *Phys. Rev. Lett.* **89** 255502

[23] Williams P A *et al* 2003 Fabrication of nanometer-scale mechanical devices incorporating individual multiwalled

carbon nanotubes as torsional springs *Appl. Phys. Lett.* **82** 805–7

[24] Thess A *et al* 1996 Crystalline ropes of metallic carbon nanotubes *Science* **273** 483–7

[25] Ebbesen T W and Ajayan P M 1992 Large-scale synthesis of carbon nanotubes *Nature* **358** 220–2

[26] Yuzvinsky T D, Fennimore A M, Kis A and Zettl A 2006 Controlled placement of highly aligned carbon nanotubes for the manufacture of arrays of nanoscale torsional actuators *Nanotechnology* **17** 434–8

[27] Hutchison J L *et al* 2001 Double-walled carbon nanotubes fabricated by a hydrogen arc discharge method *Carbon* **39** 761–70

[28] Journet C *et al* 1997 Large-scale production of single-walled carbon nanotubes by the electric-arc technique *Nature* **388** 756–8

[29] O'Connell M J *et al* 2002 Band gap fluorescence from individual single-walled carbon nanotubes *Science* **297** 593–6

[30] Meyer J C, Cech J, Hornbostel B and Roth S 2006 Progress in single-walled carbon nanotube based nanoelectromechanical systems *Phys. Status Solidi* b **243** 3500–4

[31] Li Y, Liu J, Wang Y Q and Wang Z L 2001 Preparation of monodispersed Fe–Mo nanoparticles as the catalyst for CVD synthesis of carbon nanotubes *Chem. Mater.* **13** 1008–14

[32] Qi H, Qian C and Liu J 2007 Synthesis of uniform double-walled carbon nanotubes using iron disilicide as catalyst *Nano Lett.* **7** 2417–21

[33] Bourlon B, Glattli D C, Miko C, Forró L and Bachtold A 2004 Carbon nanotube based bearing for rotational motions *Nano Lett.* **4** 709–12

[34] Robertson D H, Brenner D W and Mintmire J W 1992 Energetics of nanoscale graphitic tubules *Phys. Rev. B* **45** 12592–5

[35] Lu J P 1997 Elastic properties of carbon nanotubes and nanoropes *Phys. Rev. Lett.* **79** 1297–300

[36] Hernández E, Goze C, Bernier P and Rubio A 1998 Elastic properties of C and $B_xC_yN_z$ composite nanotubes *Phys. Rev. Lett.* **80** 4502–5

[37] Sánchez-Portal D, Artacho E, Soler J M, Rubio A and Ordejón P 1999 *Ab initio* structural, elastic, and vibrational properties of carbon nanotubes *Phys. Rev. B* **59** 12678–88

[38] Popov V N, Van Doren V E and Balkanski M 2000 Elastic properties of single-walled carbon nanotubes *Phys. Rev. B* **61** 3078–84

[39] Belytschko T, Xiao S P, Schatz G C and Ruoff R S 2002 Atomistic simulations of nanotube fracture *Phys. Rev. B* **65** 235430

[40] Sears A and Batra R C 2004 Macroscopic properties of carbon nanotubes from molecular-mechanics simulations *Phys. Rev. B* **69** 235406

[41] Yakobson B I, Brabec C J and Bernholc J 1996 Nanomechanics of carbon tubes: instabilities beyond linear response *Phys. Rev. Lett.* **76** 2511–4

[42] Kudin K N, Scuseria G E and Yakobson B I 2001 C_2F, BN, and C nanoshell elasticity from *ab initio* computations *Phys. Rev. B* **64** 235406

[43] Li C and Chou T-W 2003 Elastic moduli of multi-walled carbon nanotubes and the effect of van der Waals forces *Compos. Sci. Technol.* **63** 1517–24

[44] Shen L and Li J 2005 Transversely isotropic elastic properties of multiwalled carbon nanotubes *Phys. Rev. B* **71** 035412

[45] Jeong B W, Lim J K and Sinnott S B 2007 Torsional stiffening of carbon nanotube systems *Appl. Phys. Lett.* **91** 093102

[46] Shima H 2012 Buckling of carbon nanotubes: a state of the art review *Materials* **5** 47–84

[47] Zhang C L and Shen H S 2006 Buckling and postbuckling analysis of single-walled carbon nanotubes in thermal environments via molecular dynamics simulation *Carbon* **44** 2608–16

[48] Fang C, Kumar A and Mukherjee S 2011 A finite element analysis of single-walled carbon nanotube deformation *J. Appl. Mech.—Trans. ASME* **78** 034502

[49] Wang Q, Quek S T and Varadan V K 2007 Torsional buckling of carbon nanotubes *Phys. Lett.* A **367** 135–9

[50] Shen H S and Zhang C L 2010 Torsional buckling and postbuckling of double-walled carbon nanotubes by nonlocal shear deformable shell model *Compos. Struct.* **92** 1073–84

[51] Zhang Y Y and Wang C M 2008 Torsional responses of double-walled carbon nanotubes via molecular dynamics simulations *J. Phys.: Condens. Matter* **20** 455214

[52] Wang Q 2008 Torsional buckling of double-walled carbon nanotubes *Carbon* **46** 1172–4

[53] Arroyo M and Belytschko T 2003 Nonlinear mechanical response and rippling of thick multiwalled carbon nanotubes *Phys. Rev. Lett.* **91** 215505

[54] Wang X, Yang H K and Dong K 2005 Torsional buckling of multi-walled carbon nanotubes *Mater. Sci. Eng.* A **404** 314–22

[55] Zou J, Huang X, Arroyo M and Zhang S L 2009 Effective coarse-grained simulations of super-thick multi-walled carbon nanotubes under torsion *J. Appl. Phys.* **105** 033516

[56] Chopra N G *et al* 1995 Fully collapsed carbon nanotubes *Nature* **377** 135–8

[57] Gao G H, Cagin T and Goddard W A 1998 Energetics, structure, mechanical and vibrational properties of single-walled carbon nanotubes *Nanotechnology* **9** 184–91

[58] Liu B, Yu M F and Huang Y G 2004 Role of lattice registry in the full collapse and twist formation of carbon nanotubes *Phys. Rev. B* **70** 161402

[59] Xiao J *et al* 2007 Collapse and stability of single- and multi-wall carbon nanotubes *Nanotechnology* **18** 395703

[60] Yu M F *et al* 2001 Locked twist in multiwalled carbon-nanotube ribbons *Phys. Rev. B* **64** 241403

[61] Liang H Y and Upmanyu M 2006 Axial-strain-induced torsion in single-walled carbon nanotubes *Phys. Rev. Lett.* **96** 165501

[62] Mu W, Li M, Wang W and Ou-Yang Z-C 2009 Study of axial strain-induced torsion of single-wall carbon nanotubes using the 2D continuum anharmonic anisotropic elastic model *New J. Phys.* **11** 113049

[63] Zhang H W, Wang L, Wang J B, Zhang Z Q and Zheng Y G 2008 Torsion induced by axial strain of double-walled carbon nanotubes *Phys. Lett.* A **372** 3488–92

[64] Zhao R and Luo C 2011 Torsion-induced mechanical couplings of single-walled carbon nanotubes *Appl. Phys. Lett.* **99** 231904

[65] Chang T C 2007 Torsional behavior of chiral single-walled carbon nanotubes is loading direction dependent *Appl. Phys. Lett.* **90** 201910

[66] Gartstein Y N, Zakhidov A A and Baughman R H 2003 Mechanical and electromechanical coupling in carbon nanotube distortions *Phys. Rev. B* **68** 115415

[67] Papadakis S, Williams P, Falvo M, Superfine R and Washburn S 2003 Mechanics of nanotubes and nanotube-based devices *Molecular Nanostructures: 17th Int. Winterschool Euroconf. on Electronic Properties Of Novel Materials* **685** 577–86

[68] Papadakis S J *et al* 2004 Resonant oscillators with carbon-nanotube torsion springs *Phys. Rev. Lett.* **93** 146101

[69] Buldum A and Lu J P 1999 Atomic scale sliding and rolling of carbon nanotubes *Phys. Rev. Lett.* **83** 5050–3

[70] Palser A H R 1999 Interlayer interactions in graphite and carbon nanotubes *Phys. Chem. Chem. Phys.* **1** 4459–64

[71] Kolmogorov A N and Crespi V H 2000 Smoothest bearings: interlayer sliding in multiwalled carbon nanotubes *Phys. Rev. Lett.* **85** 4727–30

[72] DiCarlo A, Monteferrante M, Podio-Guidugli P, Sansalone V and Teresi L 2004 How (and why) twisting cycles make individual MWCNTs stiffer *AIP Conf. Proc.* **723** 355

[73] Xiao S and Hou W 2007 Studies of nanotube-based resonant oscillators through multiscale modeling and simulation *Phys. Rev.* B **75** 125414

[74] Zalamea L, Kim H and Pipes R B 2007 Stress transfer in multi-walled carbon nanotubes *Compos. Sci. Technol.* **67** 3425–33

[75] Jeong B W and Sinnott S B 2009 A torsional parametric oscillator based on carbon nanotubes *Appl. Phys. Lett.* **95** 083112

[76] Selim M M 2010 Torsional vibration of carbon nanotubes under initial compression stress *Braz. J. Phys.* **40** 283–7

[77] Khademolhosseini F, Phani A S, Nojeh A and Rajapakse R 2012 Nonlocal continuum modeling and molecular dynamics simulation of torsional vibration of carbon nanotubes *IEEE Trans. Nanotechnol.* **11** 34–43

[78] Young W C and Budynas R G 2002 *Roark's Formulas for Stress and Strain* (New York: McGraw-Hill)

[79] Xiao S and Hou W 2007 Multiscale modeling and simulation of nanotube-based torsional oscillators *Nanoscale Res. Lett.* **2** 54–9

[80] Guo W, Zhong W, Dai Y and Li S 2005 Coupled defect-size effects on interlayer friction in multiwalled carbon nanotubes *Phys. Rev.* B **72** 075409

[81] Tsetseris L and Pantelides S T 2011 Defect formation and hysteretic inter-tube displacement in multi-wall carbon nanotubes *Carbon* **49** 581–6

[82] Tsetseris L and Pantelides S T 2011 Defect-related hysteresis in nanotube-based nano-electromechanical systems *Nanoscale Res. Lett.* **6** 245

[83] Nagapriya K S *et al* 2008 Origin of torsion-induced conductance oscillations in carbon nanotubes *Phys. Rev.* B **78** 165417

[84] Garcia-Sanchez D *et al* 2007 Mechanical detection of carbon nanotube resonator vibrations *Phys. Rev. Lett.* **99** 085501

[85] Carr D W, Evoy S, Sekaric L, Craighead H G and Parpia J M 1999 Measurement of mechanical resonance and losses in nanometer scale silicon wires *Appl. Phys. Lett.* **75** 920–2

[86] Hall A R, Falvo M R, Superfine R and Washburn S 2008 A self-sensing nanomechanical resonator built on a single-walled carbon nanotube *Nano Lett.* **8** 3746–9

[87] Nagapriya K S *et al* 2008 Torsional stick-slip behavior in WS$_2$ nanotubes *Phys. Rev. Lett.* **101** 195501

[88] Yu M F, Yakobson B I and Ruoff R S 2000 Controlled sliding and pullout of nested shells in individual multiwalled carbon nanotubes *J. Phys. Chem.* B **104** 8764–7

[89] Kis A, Jensen K, Aloni S, Mickelson W and Zettl A 2006 Interlayer forces and ultralow sliding friction in multiwalled carbon nanotubes *Phys. Rev. Lett.* **97** 025501

[90] Meyer J C, Paillet M and Roth S 2005 Single-molecule torsional pendulum *Science* **309** 1539–41

[91] Hall A R 2006 Experimental measurement of single-wall carbon nanotube torsional properties *Phys. Rev. Lett.* **96** 256102

[92] Hall A R *et al* 2010 Experimental measurement of single-wall carbon nanotube torsional properties [*Phys. Rev. Lett.* **96** 256102 (2006)] *Phys. Rev. Lett.* **105** 69904 (erratum)

[93] Lin L, Cui T, Qin L-C and Washburn S 2011 Direct measurement of the friction between and shear moduli of shells of carbon nanotubes *Phys. Rev. Lett.* **107** 206101

[94] Yao N and Lordi V 1998 Young's modulus of single-walled carbon nanotubes *J. Appl. Phys.* **84** 1939

[95] Ajiki H and Ando T 1995 Lattice distortion of metallic carbon nanotubes by induced magnetic fields *J. Phys. Soc. Japan* **64** 260–7

[96] Charlier A, McRae E, Heyd R and Charlier M F 2001 Metal–semiconductor transitions under uniaxial stress for single- and double-walled carbon nanotubes *J. Phys. Chem. Solids* **62** 439–44

[97] Lu J P 1995 Novel magnetic properties of carbon nanotubes *Phys. Rev. Lett.* **74** 1123–6

[98] Mehrez H, Svizhenko A, Anantram M P, Elstner M and Frauenheim T 2005 Analysis of band-gap formation in squashed armchair carbon nanotubes *Phys. Rev.* B **71** 155421

[99] Nakanishi T and Ando T 2006 Aharonov–Bohm effects on conductivity in carbon nanotubes: a tool for determination of a gap due to strain and curvature *Phys. Status Solidi* b **243** 3370–4

[100] Saito R, Dresselhaus G and Dresselhaus M S 1993 Electronic structure of double-layer graphene tubules *J. Appl. Phys.* **73** 494–500

[101] Sangalli D and Marini A 2011 Anomalous Aharonov–Bohm gap oscillations in carbon nanotubes *Nano Lett.* **11** 4052–7

[102] Heyd R, Charlier A and McRae E 1997 Uniaxial-stress effects on the electronic properties of carbon nanotubes *Phys. Rev.* B **55** 6820–4

[103] Kane C L and Mele E J 1997 Size, shape, and low energy electronic structure of carbon nanotubes *Phys. Rev. Lett.* **78** 1932–5

[104] Yang L, Anantram M P, Han J and Lu J P 1999 Band-gap change of carbon nanotubes: effect of small uniaxial and torsional strain *Phys. Rev.* B **60** 13874–8

[105] Yang L and Han J 2000 Electronic structure of deformed carbon nanotubes *Phys. Rev. Lett.* **85** 154–7

[106] Bogár F, Mintmire J W, Bartha F, Mezõ T and Alsenoy C V 2005 Density-functional study of the mechanical and electronic properties of narrow carbon nanotubes under axial stress *Phys. Rev.* B **72** 085452

[107] Park C-J, Kim Y-H and Chang K J 1999 Band-gap modification by radial deformation in carbon nanotubes *Phys. Rev.* B **60** 10656–9

[108] Buttiker M, Imry Y, Landauer R and Pinhas S 1985 Generalized many-channel conductance formula with application to small rings *Phys. Rev.* B **31** 6207–15

[109] Chico L, Crespi V H, Benedict L X, Louie S G and Cohen M L 1996 Pure carbon nanoscale devices: nanotube heterojunctions *Phys. Rev. Lett.* **76** 971–4

[110] Zhou C, Kong J and Dai H 2000 Intrinsic electrical properties of individual single-walled carbon nanotubes with small band gaps *Phys. Rev. Lett.* **84** 5604–7

[111] Cao J, Wang Q and Dai H 2003 Electromechanical properties of metallic, quasimetallic, and semiconducting carbon nanotubes under stretching *Phys. Rev. Lett.* **90** 157601

[112] Minot E D *et al* 2003 Tuning carbon nanotube band gaps with strain *Phys. Rev. Lett.* **90** 156401

[113] Mann D, Javey A, Kong J, Wang Q and Dai H 2003 Ballistic transport in metallic nanotubes with reliable Pd Ohmic contacts *Nano Lett.* **3** 1541–4

[114] Javey A, Guo J, Wang Q, Lundstrom M and Dai H 2003 Ballistic carbon nanotube field-effect transistors *Nature* **424** 654–7

[115] Tombler T W 2000 Reversible electromechanical characteristics of carbon nanotubes under local-probe manipulation *Nature* **405** 769–72

[116] Stampfer C 2006 Nano-electromechanical displacement sensing based on single-walled carbon nanotubes *Nano Lett.* **6** 1449–53

[117] Hall A R, Falvo M R, Superfine R and Washburn S 2007 Electromechanical response of single-walled carbon nanotubes to torsional strain in a self-contained device *Nature Nanotechnol.* **2** 413–6

[118] Fisher D S and Lee P A 1981 Relation between conductivity and transmission matrix *Phys. Rev.* B **23** 6851–4

[119] Lunde A M, Flensberg K and Jauho A-P 2005 Intershell resistance in multiwall carbon nanotubes: a Coulomb drag study *Phys. Rev.* B **71** 125408

[120] Kociak M *et al* 2002 Linking chiral indices and transport properties of double-walled carbon nanotubes *Phys. Rev. Lett.* **89** 155501

[121] Wang S and Grifoni M 2008 Transport properties of double-walled carbon nanotube quantum dots *Phys. Rev.* B **77** 085431

[122] Triozon F, Roche S, Rubio A and Mayou D 2004 Electrical transport in carbon nanotubes: role of disorder and helical symmetries *Phys. Rev.* B **69** 121410

[123] Frank S, Poncharal P, Wang Z L and Heer W A d 1998 Carbon nanotube quantum resistors *Science* **280** 1744–6

[124] Urbina A, Echeverría I, Pérez-Garrido A, Díaz-Sánchez A and Abellán J 2003 Quantum conductance steps in solutions of multiwalled carbon nanotubes *Phys. Rev. Lett.* **90** 106603

[125] Gómez-Navarro C, Sáenz J J and Gómez-Herrero J 2006 Conductance oscillations in squashed carbon nanotubes *Phys. Rev. Lett.* **96** 1–4

[126] Paulson S *et al* 1999 *In situ* resistance measurements of strained carbon nanotubes *Appl. Phys. Lett.* **75** 2936–8

[127] Collins P C, Arnold M S and Avouris P 2001 Engineering carbon nanotubes and nanotube circuits using electrical breakdown *Science* **292** 706–9

[128] Bethune D S *et al* 1993 Cobalt-catalyzed growth of carbon nanotubes with single-atomic-layer walls *Nature* **363** 605–7

[129] Qin L-C 2006 Electron diffraction from carbon nanotubes *Rep. Prog. Phys.* **69** 2761–821

[130] Qin L-C 1994 Electron diffraction from cylindrical nanotubes *J. Mater. Res.* **9** 2450–6

[131] Lucas A A, Bruyninckx V and Lambin P 1996 Calculating the diffraction of electrons or X-rays by carbon nanotubes *Europhys. Lett.* **35** 355–60

[132] Lambin P and Lucas A A 1997 Quantitative theory of diffraction by carbon nanotubes *Phys. Rev.* B **56** 3571–4

[133] Cowley J M, Nikolaev P, Thess A and Smalley R E 1997 Electron nano-diffraction study of carbon single-walled nanotube ropes *Chem. Phys. Lett.* **265** 379–84

[134] Liu Z J and Qin L-C 2005 A direct method to determine the chiral indices of carbon nanotubes *Chem. Phys. Lett.* **408** 75–9

[135] Qin L-C 1998 Measuring the true helicity of carbon nanotubes *Chem. Phys. Lett.* **297** 23–8

[136] Qin L-C, Ichihashi T and Iijima S 1997 On the measurement of helicity of carbon nanotubes *Ultramicroscopy* **67** 181–9

[137] Qin L-C *et al* 1997 Helicity and packing of single-walled carbon nanotubes studied by electron nanodiffraction *Chem. Phys. Lett.* **268** 101–6

[138] Gao M *et al* 2003 Structure determination of individual single-wall carbon nanotubes by nanoarea electron diffraction *Appl. Phys. Lett.* **82** 2703–5

[139] Liu Z J, Zhang Q and Qin L-C 2005 Accurate determination of atomic structure of multiwalled carbon nanotubes by nondestructive nanobeam electron diffraction *Appl. Phys. Lett.* **86** 191903

[140] Qin L-C 2007 Determination of the chiral indices (*n*,*m*) of carbon nanotubes by electron diffraction *Phys. Chem. Chem. Phys.* **9** 31–48

[141] Deniz H, Derbakova A and Qin L-C 2010 A systematic procedure for determining the chiral indices of multi-walled carbon nanotubes using electron diffraction-each and every shell *Ultramicroscopy* **111** 66–72

[142] Liu Z J and Qin L-C 2005 A practical approach to determine the handedness of chiral carbon nanotubes by electron diffraction *Chem. Phys. Lett.* **405** 265–9

[143] Fu Q, Huang S M and Liu J 2004 Chemical vapor depositions of single-walled carbon nanotubes catalyzed by uniform Fe_2O_3 nanoclusters synthesized using diblock copolymer micelles *J. Phys. Chem.* B **108** 6124–9

[144] Huang S M, Cai X Y, Du C S and Liu J 2003 Oriented long single walled carbon nanotubes on substrates from floating catalysts *J. Phys. Chem.* B **107** 13251–4

[145] Lin L 2011 Fabrication, structure and properties of a single carbon nanotube-based nanoelectromechanical system *PhD Thesis* University of North Carolina at Chapel Hill

[146] Lin L, Cui T, Qin L-C and Washburn S 2011 Direct measurement of the friction between and shear moduli of shells of carbon nanotubes *Phys. Rev. Lett.* **107** 206101

[147] Shibutani Y and Ogata S 2004 Mechanical integrity of carbon nanotubes for bending and torsion *Modelling Simul. Mater. Sci. Eng.* **12** 599–610

[148] Liu Z J and Qin L-C 2005 Measurement of handedness in multiwalled carbon nanotubes by electron diffraction *Chem. Phys. Lett.* **411** 291–6

[149] Margulis L, Dluzewski P, Feldman Y and Tenne R 1996 TEM study of chirality in MoS_2 nanotubes *J. Microsc.—Oxford* **181** 68–71

[150] Saran N *et al* 2004 Fabrication and characterization of thin films of single-walled carbon nanotube bundles on flexible plastic substrates *J. Am. Chem. Soc.* **126** 4462–3

[151] Zhang D *et al* 2006 Transparent, conductive, and flexible carbon nanotube films and their application in organic light-emitting diodes *Nano Lett.* **6** 1880–6

[152] Cao Q *et al* 2008 Medium-scale carbon nanotube thin-film integrated circuits on flexible plastic substrates *Nature* **454** 495–500

[153] Chowdhury R, Adhikari S and Mitchell J 2009 Vibrating carbon nanotube based bio-sensors *Physica* E **42** 104–9

[154] Li C Y and Chou T W 2004 Mass detection using carbon nanotube-based nanomechanical resonators *Appl. Phys. Lett.* **84** 5246–8

[155] Pesetski A A *et al* 2008 A 500 MHz carbon nanotube transistor oscillator *Appl. Phys. Lett.* **93** 123506

[156] Cornwell C F and Wille L T 1997 Elastic properties of single-walled carbon nanotubes in compression *Solid State Commun.* **101** 555–8

[157] Krishnan A, Dujardin E, Ebbesen T W, Yianilos P N and Treacy M M J 1998 Young's modulus of single-walled nanotubes *Phys. Rev.* B **58** 14013–9

[158] Ozaki T, Iwasa Y and Mitani T 2000 Stiffness of single-walled carbon nanotubes under large strain *Phys. Rev. Lett.* **84** 1712–5

[159] Van Lier G, Van Alsenoy C, Van Doren V and Geerlings P 2000 *Ab initio* study of the elastic properties of single-walled carbon nanotubes and graphene *Chem. Phys. Lett.* **326** 181–5

[160] Shen L and Li J 2004 Transversely isotropic elastic properties of single-walled carbon nanotubes *Phys. Rev.* B **69** 045414

[161] Pullen A, Zhao G L, Bagayoko D and Yang L 2005 Structural, elastic, and electronic properties of deformed carbon nanotubes under uniaxial strain *Phys. Rev.* B **71** 205410

[162] Gupta S, Dharamvir K and Jindal V K 2005 Elastic moduli of single-walled carbon nanotubes and their ropes *Phys. Rev.* B **72** 165428